

---

# ROBUST QUANTUM DOTS CHARGE AUTOTUNING USING NEURAL NETWORKS UNCERTAINTY

---

A PREPRINT

 **Victor Yon**<sup>\*1,2,3</sup>,  **Bastien Galaup**<sup>1,2,3</sup>,  **Claude Rohrbacher**<sup>2,3,4</sup>,  **Joffrey Rivard**<sup>2,3,4</sup>,  **Clément Godfrin**<sup>5</sup>,  
 **Ruoyu Li**<sup>5</sup>,  **Stefan Kubicek**<sup>5</sup>,  **Kristiaan De Greve**<sup>5</sup>,  **Louis Gaudreau**<sup>6</sup>,  **Eva Dupont-Ferrier**<sup>2,3,4</sup>,  
 **Yann Beilliard**<sup>1,2,3</sup>,  **Roger G. Melko**<sup>7,8</sup>, and  **Dominique Drouin**<sup>1,2,3</sup>

<sup>1</sup>Institut Interdisciplinaire d'Innovation Technologique (3iT), Université de Sherbrooke, Sherbrooke, QC, Canada, J1K 0A5

<sup>2</sup>Laboratoire Nanotechnologies Nanosystèmes (LN2) — CNRS 3463, Université de Sherbrooke, Sherbrooke, QC, Canada, J1K 0A5

<sup>3</sup>Institut quantique (IQ), Université de Sherbrooke, Sherbrooke, QC, Canada, J1K 2R1

<sup>4</sup>Département de physique, Université de Sherbrooke, Sherbrooke, QC, Canada, J1K 2R1

<sup>5</sup>IMEC, Kapeldreef 75, 3001 Leuven, Belgium

<sup>6</sup>National Research Council Canada, Quantum and Nanotechnologies Research Center, ON, Ottawa, Canada, K1A 0R6

<sup>7</sup>Department of Physics and Astronomy, University of Waterloo, Waterloo, ON, Canada, N2L 3G1

<sup>8</sup>Perimeter Institute for Theoretical Physics, Waterloo, ON, Canada, N2L 2Y5

August 21, 2024

## ABSTRACT

This study presents a machine-learning-based procedure to automate the charge tuning of semiconductor spin qubits with minimal human intervention, addressing one of the significant challenges in scaling up quantum dot technologies. This method exploits artificial neural networks to identify noisy transition lines in stability diagrams, guiding a robust exploration strategy leveraging neural networks' uncertainty estimations. Tested across three distinct offline experimental datasets representing different single quantum dot technologies, the approach achieves over 99 % tuning success rate in optimal cases, where more than 10 % of the success is directly attributable to uncertainty exploitation. The challenging constraints of small training sets containing high diagram-to-diagram variability allowed us to evaluate the capabilities and limits of the proposed procedure.

**Keywords** Artificial Neural Networks · Bayesian Neural Networks · Quantum Dots · Charge Autotuning · Uncertainty Estimation

## 1 Introduction

Multiple quantum computing technologies compete to outperform classical computers for practical applications, yet the journey toward this objective is fraught with considerable technical challenges. This article specifically studies quantum systems based on semiconductor spin qubits [1–4], formed by electrostatically confining electrons in quantum dots (QDs). This technology presents several advantages, such as high-gate fidelity [5–9], long coherence time [10, 11], thermal robustness at temperatures greater than one kelvin [12], and compatibility with well-established complementary metal-oxide-semiconductor (CMOS) technology [13, 14]. This compatibility further amplifies scalability potential and enables co-integration with industrial electronics [15, 16]. However, QD technology is still in an early stage of development, the best materials [17, 18], fabrication techniques, use cases, and control procedures are yet to be discovered.

One bottleneck to the large-scale implementation of quantum computers based on QDs is the complexity of charge tuning, one of the preliminary tasks required to set up a qubit. This tuning task consists in confining a specific number

---

\*victor.yon@usherbrooke.ca

of charge carriers in one or multiple QDs using the information provided by indirect measurements, which is typically obtained by tuning the voltages at two control gates (G1 and G2 in Figure 1). The result of voltages sweeping can be visualized as 2-dimensional images, named stability diagrams (examples in Figure 2a,b,c), where pixels encode the current measured with a single-electron transistor (SET) [19] or a quantum point contact (QPC) [20]. One could then identify the transition lines (highlighted with green lines in Figure 2d,e,f) that represent a change in the number of charge carriers inside the QD. Associated with the knowledge that electron-based QDs are empty at low gate voltage, it is possible to deduce the number of charges for each area of the voltage space (blue areas in Figure 2d,e,f).

However, the task is challenging to automate because stability diagrams' parameter space is vast, noisy, and device-dependent. For this reason, tuning the number of charges inside the QD is usually done manually by experimentalists, based on informed guesses and human heuristics. While this approach is sufficient for small proof-of-concepts in research laboratories, it is incompatible with large-scale industrial applications. Moreover, measuring a large area of a stability diagram could take hours, which significantly slows down the QD initialization, especially since it often requires iterative measurements. One could attempt to automate the tuning procedure with classical algorithms and human expertise [21], but such an approach still requires humans in the loop and is tailored to specific hardware. Thus, it does not satisfy the requirement for scaling up the technology or accelerating the development of new designs.

Recent works [22, 23] suggested automating the tuning procedure using a machine learning (ML) approach with artificial deep neural networks (NNs) [24]. These methods show promising results but are not yet reliable enough to consider fully autonomous large-scale QD control. The relatively high failure rate of these ML approaches (25 % [22] for single QD and 43 % [23] for double QD charge tuning) could be attributed to (i) the overconfidence of the model while facing ambiguous, out-of-distribution, too small, or noisy measurements and (ii) the low error-tolerance of the exploration strategy. For example, one transition line misdetection will often lead to the failure of the whole charge tuning procedure. In the context of coarse tuning, Ziegler et al. [25] addressed a similar issue by training a first NN to evaluate the measurement quality before sending it to a second NN to infer the class. Ziegler et al. [26] combined this method with custom peak-finding techniques to tune offline double QD into a specific charge regime with 89.7 % accuracy. Here, we chose a more versatile approach by training a single NN to detect the transition lines and providing a classification confidence score at the same time. One could also improve the ML models performance with more parameters and a larger dataset, but a very large model could be challenging to integrate near the tuned devices, and the high cost of collecting more diagrams is prohibitive. Even so, ML models never come with the guarantee of perfect accuracy.

This study introduces a hardware-agnostic autotuning procedure that leverages NN uncertainty to significantly enhance the robustness of semiconductor spin qubit charge tuning with minimal human intervention. It is achieved by training an NN to identify transition lines in a stability diagram with supervised learning, coupled with an exploration strategy incorporating the NN's predictions and confidence score (measure of uncertainty). We considered two methods to estimate the confidence score of an NN, one with a heuristic from classical NNs and one using the Bayesian framework applied to NNs [27, 28]. Those two methods have been evaluated by their concrete ability to reduce critical failure rate during the autotuning procedure over three different experimental offline datasets measured on different single QD hardware.

## 2 Problem definition

### 2.1 Project scope

Before using QDs as qubits to perform operations, each QD has to be tuned into a specific charge state by applying appropriate gate voltages. The complete calibration procedure can be divided into five distinct steps: (i) *bootstrapping*: cooling the device and bringing its regime into the appropriate parameter range ; (ii) *coarse tuning* [25, 26, 29–34]: tuning the QDs into a specific topology (e.g., single QD, double QD) ; (iii) *establishing controllability* [26, 29, 35, 36]: setup virtual gates that compensate capacitive cross-talk ; (iv) *charge state tuning* [22, 23, 26, 37]: tuning the QDs into specific charge configuration (number of electrons in our case) ; (v) *fine-tuning* [29, 38]: adjusting the inter-dot tunnel coupling. For a more detailed description of these steps, refer to Zwolak and Taylor [39]. Performing these tasks quickly and reliably is one of the technical challenges preventing the scale-up of the number of qubits in QD-based quantum computers.

This work focuses on automating the task of charge state tuning (iv). We assume the system is bootstrapped (i) and the voltage range contains a single QD (ii). However, our method does not require setting up virtual gates (iii) since we opted for a flexible approach by detecting the slope of the transition lines during the procedure.

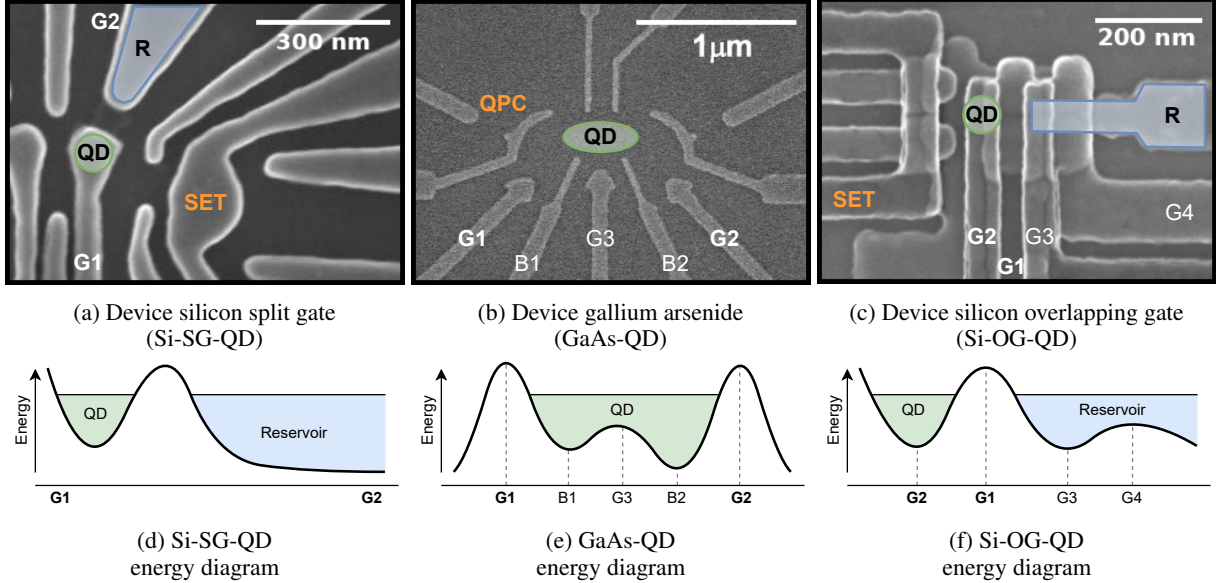


Figure 1: Quantum dot (QD) devices used to measure the stability diagrams. **(a,b,c)** Scanning electron microscope (SEM) images of experimental devices. A single-QD can be created by tuning electrostatic gate 1 (G1) and 2 (G2) to appropriate voltages. **(a)** G2 controls the electronic density of an electron reservoir (R), and the single-electron transistor (SET) is used as a charge sensor. See [40] for experimental details. **(b)** The tunnel barriers labeled B1 and B2 are set to a fixed voltage, as well as gate 3 (G3) which is required for more than one QD only. The quantum point contact (QPC) is used as a charge sensor. See [41] for experimental details. **(c)** G1 and G4 are tunnel barriers. The voltages at G3, G4, and R are fixed to allow single-QD formation under G2 and an extended reservoir. The SET is used as a charge sensor. See [14] for experimental details. **(d,e,f)** Energy diagrams representing the formation of a single-QD for each device.

## 2.2 Problem frame and constraints

We framed the problem of charge state tuning as an exploration task where each step consists of detecting charge transition lines in the measurement of a voltage space subsection. The ultimate goal is to reach a specific charge regime while minimizing the exploration cost. In this case, the cost is the measurement time, which is directly affected by the number of steps and the size of the subsection measured. This approach allows us to break down the problem into two distinct tasks: the transition line detection (Section 3) and the diagram exploration strategy (Section 4).

To uphold the robustness and adaptability of our methodology, we consciously minimized the utilization of pre-processing techniques while maintaining a relatively simple NN model. This decision is grounded in the ultimate objective of implementing this solution on custom electronics inside the cryogenic environment of a dilution refrigerator to perform in-situ online tuning. The computational constraints and the need for a streamlined process inherent to this environment necessitate a careful balance between model complexity and operational energy efficiency. To evaluate the efficacy of our approach across various QD designs, we tested our method on three distinct datasets, each obtained from a different hardware and research group. This ensures that our solution is not tailored specifically to one quantum device but can be applied to a wide range of QD-based spin qubit hardware.

## 2.3 Datasets

We tested our approach on offline experimental measurements obtained from three different QD device architectures on distinct experimental setups. The first dataset, referred to as silicon split gate (Si-SG-QD) [40], contains 17 stability diagrams (Figure 2a) measured from devices fabricated with metal-oxide-semiconductor (MOS) single-layer architecture (Figure 1a). The second dataset, referred to as gallium arsenide (GaAs-QD) [41], is composed of 9 stability diagrams (Figure 2b) obtained by measuring the current of a device fabricated with GaAs/AlGaAs heterostructure (Figure 1b). The third and last dataset, referred to as silicon overlapping gate (Si-OG-QD) [14], includes 12 stability diagrams (Figure 2c) measured from devices fabricated with MOS stacked layers architecture (Figure 1c). The diagrams from the first and the third datasets are measured with a SET, while the ones from the second dataset are measured with a QPC. The measurements are two-dimensional stability diagrams represented as images, where the  $x$  and  $y$

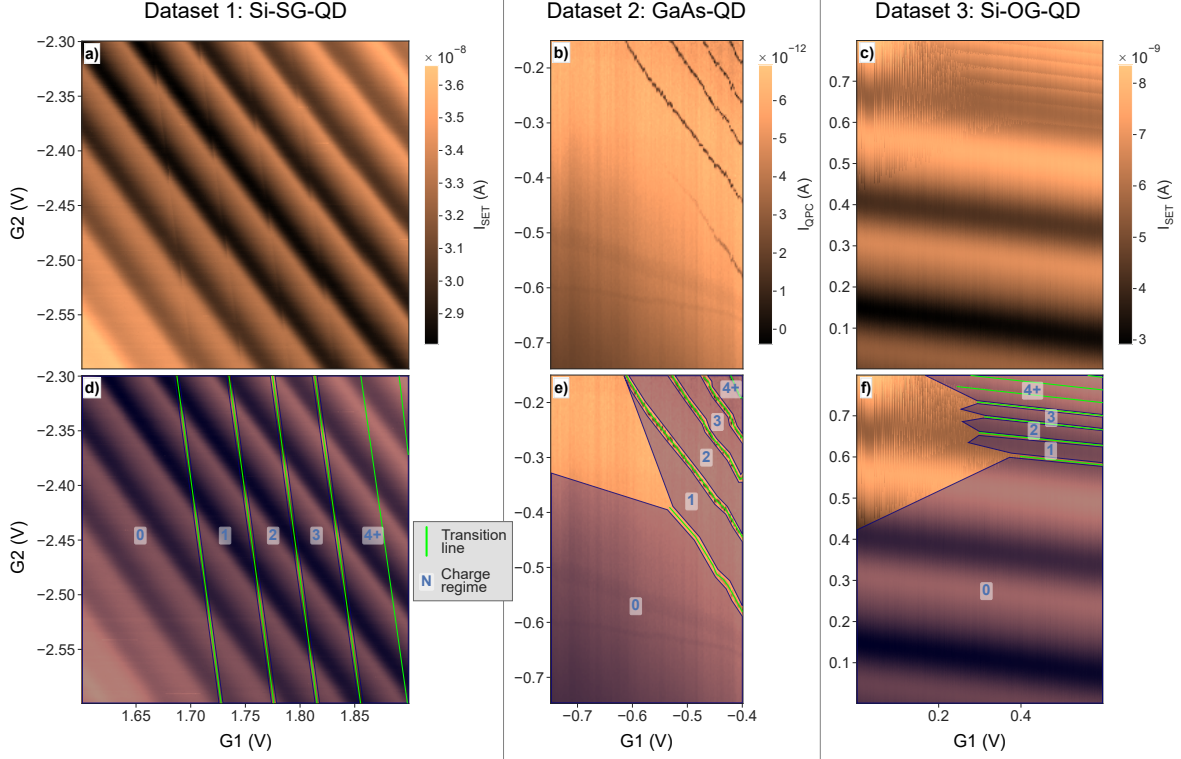


Figure 2: Example of one stability diagram from each dataset. **(a,b,c)** Representation of the stability diagrams as image, where pixels encode the measured current for given voltage values at the gates (G1 and G2). **(d,e,f)** Same diagrams with manual annotations of transition lines in green and charge regime areas in blue. The regions with more than 3 charges are grouped under the annotation “4+”. A voltage area not annotated with a charge regime, due to fading line or ambiguous boundary, is considered as “unknown charge regime”. More examples can be found in the supplementary Section S1.6.

axes correspond to voltages swiped respectively at the gates G1 and G2. If more than two gates are available in the experimental setup, the other ones are fixed to a voltage compatible with a single QD regime.

Using simulated stability diagrams could increase the size of the training set [33, 42] but at the cost of a distribution shift between the train and test sets, which could harm the quality of uncertainty quantification. We therefore chose to rely exclusively on experimental data. We also minimized measurement pre-processing to ensure compatibility with a future in-situ online implementation of this autotuning method. Only input normalization is applied to the measured patch before being sent to the classification model. See supplementary Section S1 for detailed dataset preparation and diagram selection.

Each dataset features different defect, noise, and transition line patterns that create a large variety of challenges for the autotuning procedure. The diagrams from Si-SG-QD present a strong oscillating background noise caused by cross-capacitance effects of G1 and G2 acting on the SET, which can be hard to differentiate from the transition lines (see diagonal parasitic oscillations in Figure 2a). Therefore, the most challenging part of tuning such devices resides in reliably detecting the lines, especially in low and high current areas. The challenge is entirely different with diagrams from the GaAs-QD dataset, where the transition lines are usually easy to identify but can fade (see first line in Figure 2b) and curve unexpectedly. This specificity moves the challenge to the exploration task, where missing a fading line can lead to a wrong number of charges in the QD. Finally, diagrams from Si-OG-QD present a peculiar hysteresis noise when the reservoir tunneling rate is slower than the voltage sweeping speed (see top left in Figure 2c), which must be correctly classified by the model and taken into account by the exploration strategy. The supplementary Section S1.6 presents a diagram sample of each dataset, and every measurement file used to generate the diagrams of the present study can be downloaded from Yon et al. [43].

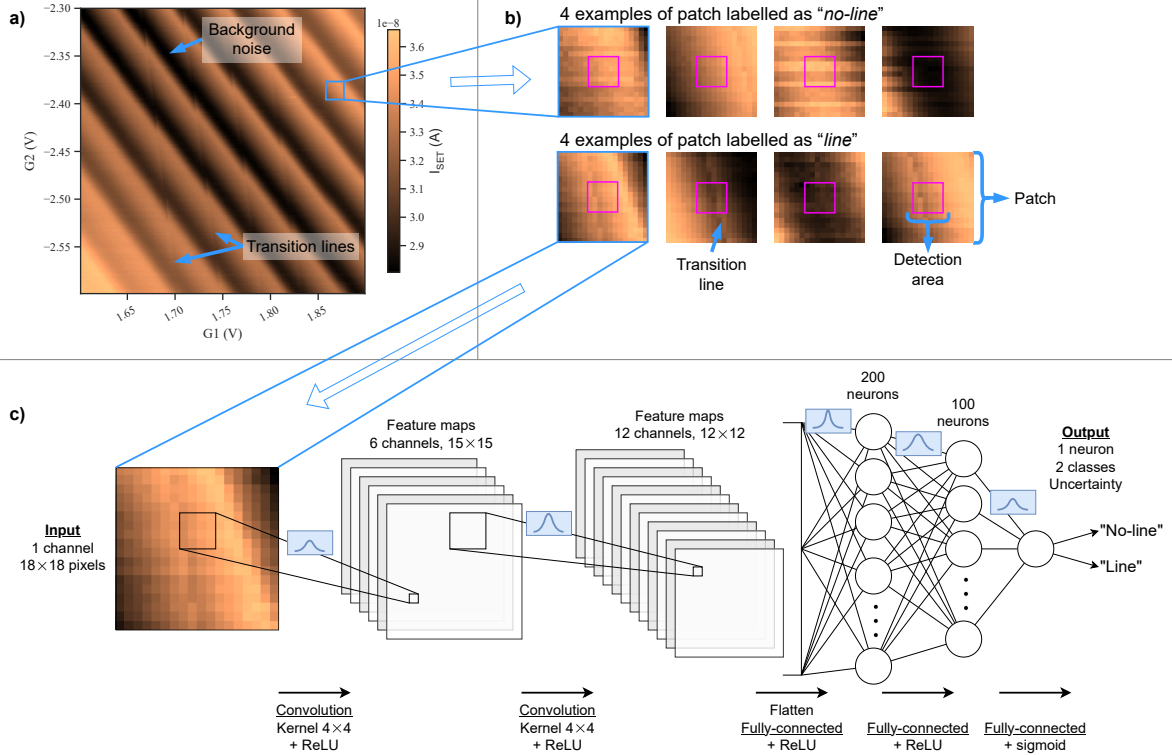


Figure 3: Automatic transition line detection with a Bayesian convolutional neural network (BCNN) in a stability diagram. **(a)** A subsection (patch) of the voltage space is measured. This diagram presents strong oscillating background noise that should not be misinterpreted as a transition line. **(b)** To train the model, each patch is categorized as “line” if a transition line annotation intersects with the detection area (in pink) in the center of the patch. Otherwise, the patch is categorized as “no-line”. **(c)** The patch is then sent as input of a model, where a forward-pass propagates the information through convolutional and fully-connected layers. In this example, a BCNN is represented, in which each parameter is encoded as a Gaussian distribution.

### 3 Line detection

#### 3.1 Method

The first part of the procedure consists of automatically detecting charge transition lines in subsections of offline experimental stability diagrams (Figure 3). An image segmentation model [44, 45] could identify lines, but it would require scanning large diagram sections, which is expected to slow down the autotuning process. To relax the input size requirement and reduce the model complexity, we address this problem as a supervised binary classification task (“line” or “no-line”). The choice of NN rather than alternative statistical methods is firstly driven by the goal of designing a hardware-agnostic method that can adapt to the rapidly evolving QD research field. ML algorithms can automatically adjust to new data features, such as a new artifact caused by a novel measurement setup or new transition line patterns induced by a change in the QD hardware design. NN methods also have the potential to employ transfer learning methods [46] to facilitate swift adaptation of the model to newly introduced devices. Furthermore, NNs have demonstrated outstanding performance in detecting patterns within images and filtering various types of noise, especially convolutional neural networks (CNNs) [47]. Therefore, they are well suited for detecting lines within images, such as transition lines in 2-dimensional stability diagrams. Finally, NNs are known to maintain good scalability [48] with respect to the problem size and complexity, a crucial characteristic as we aim to develop a solution compatible with large arrays of QDs.

For this classification problem, we evaluated the performance of three NN architectures, CNNs, Bayesian convolutional neural networks (BCNNs), and feed-forward neural networks (FFs). CNNs are known for their effectiveness in image classification tasks [47] and provide a good tradeoff between complexity and performance. BCNNs are expected to offer robust uncertainty estimation [49, 50], which can be beneficial for improving the reliability of automatic charge-tuning

procedures. The BCNNs implement the variational inference [51, 52] method with the Bayes-by-Backprop [53] learning rule. Meanwhile, the simpler FF is a reference for comparison with the more complex CNN and BCNN models.

All NNs presented in this article are fed with the same inputs and have comparable binary outputs. The model input is a small subsection of the voltage space (also referred to as a patch), where pixels represent the measured current values. The patch size has been fixed to  $18 \times 18$  data points as an empirical tradeoff between the measurement speed and the model accuracy. The patches are generated by splitting the diagrams into evenly spaced squares and then distributed in training, validation, and testing sets. Where testing patches are extracted from a unique diagram excluded from the training set, and the other patches are randomly distributed between the training (90%) and the validation (10%) sets. Each patch is automatically classified as “*line*” if an annotation of transition line intersects the detection area in its center (Figure 3b). This labeling approach provides more context to the NN while keeping the classification window narrow enough to fit between two transition lines.

The most basic NN used here is the FF, which propagates the input through two fully connected layers. The CNN extends this model by adding two convolution layers before the fully connected layers. The BCNN architecture is identical to the CNN, with each free parameter (weights and biases) encoded as a Gaussian distribution, defined by a mean and a variance (Figure 3c). Every model is trained to infer the patch class as a binary output and express the uncertainty of this classification as a confidence percentage. More technical details about the data processing, manual diagram annotation, automatic patch labeling, and NN meta-parameters can be found in the supplementary Sections S1 and S2.

Introducing a confidence score into our model provides an additional layer of information about the model’s predictions, which we leverage at the exploration level to significantly reduce the impact of misclassifications that are usually responsible for the disruption of the autotuning procedure. We distinguish between three types of uncertainties [54, 55]:

1. Model uncertainty (a.k.a. epistemic or systemic uncertainty) arises from a lack of knowledge due to imperfect training. In the context of transition line detection, this could be due to non-optimal meta-parameters, or a low number of training diagrams. This type of uncertainty can be reduced as the model is exposed to more data, highlighting the importance of a comprehensive training process. In practice, the size of the training dataset is restrained by the acquisition cost of experimental stability diagrams.
2. Data uncertainty (a.k.a. aleatoric or statistical uncertainty), on the other hand, is associated with the inherently stochastic nature of the tested data. For the line classification task, this could result from variability in measurement tools, fabrication imperfections, or cross-talk, among others. Those factors are often out of the experimentalist’s control.
3. Finally, distributional uncertainty arises from the inadequate representation of the test set within the training set. In the context of line classification, this can occur when the stability diagram used for testing presents noise or features not present in the training set. Not using synthetic data helps us mitigate this type of uncertainty, but diagram-to-diagram variability is a source of distributional uncertainty that can never be entirely avoided.

The computation of the confidence score is handled differently between standard (CNN or FF) and Bayesian NNs. For a standard NN with an output  $y$ , we employ a simple heuristic score (Formula 1) to estimate uncertainty based on the distance between the output of the NN and the expected class [56, 57]. In the case of BCNNs, we compute the normalized standard deviation (Formula 2) based on  $N$  repeated inferences with new sampled parameters. Both formulas are trivial in the case of binary classification with one output neuron, but they can be generalized to multi-class problems [56].

$$\text{Heuristic confidence score} = |0.5 - y| \times 2 \quad (1)$$

$$\text{Bayesian confidence score} = 1 - (\text{std}(y_1, y_2, \dots, y_N) \times 2) \quad (2)$$

In addition, we performed a calibration step to optimize the exploration-exploitation tradeoff [58, 85]. Calibrating an NN is typically done with regularization methods during the training or by empirically scaling individual bins of the reliability diagram after the training [54, 59–61] to ensure that the confidence score is a good approximation of the actual probability of correctness. For example, among all classifications rated with 80% confidence, 20% of them are expected to be incorrect. In our case, the validation set does not consistently cover the range of confidence scores due to the low number of classification errors in some cases (e.g., the middle panel of the supplementary Figure S6b). This constraint makes the computation of calibration metrics unreliable, specifically with bin-based approaches. We have worked around this problem by calibrating the confidence thresholds instead of the model confidence scores. The threshold defines the confidence value under which the classification will be considered too uncertain to be trusted



during the stability diagram exploration. After each training, the threshold value is optimized by minimizing the score defined by Formula 3 with a grid search on the validation set. The goal is to find an optimal tradeoff between the number of errors above the threshold (Err) and the total number of samples under the threshold (UT), where  $\tau$  is a meta-parameter that defines the target ratio (fixed to 0.2 in this study). This approach relaxes the requirement regarding the number of calibration samples while maintaining the practical functionality of the confidence score. More details about the calibration process can be found in the supplementary Section S2.2.

$$\text{Threshold score} = \text{Err} + \text{UT} \times \tau \quad (3)$$

### 3.2 Results

With appropriate meta-parameters (supplementary Table S2), the line classification task reached more than 90% accuracy on every dataset and model combination (Table 1). The most significant performance difference between NN architectures is visible in the Si-SG-QD dataset, where convolution layers are necessary to filter the oscillating parasitic background. With GaAs-QD and Si-OG-QD datasets, the benefit of the convolution is less evident since the measurement noise is lower and the transition lines are often clearly visible. On every dataset, the classification performance of the Bayesian CNN is close to that of their classical counterparts, but the additional complexity of the Bayesian layers slows down the training by a factor of 4 on average. No overfitting was observed during the training (supplementary Figure S5), suggesting that the dropout of the classical layers and the Bayesian layers act both as efficient regularization methods.

A qualitative analysis of the misclassified patches sample (Figure 4 and supplementary Section S2.3) suggests we approach an optimal classification rate for each dataset even if the model accuracy never reaches 100%. The remaining errors are often caused by ambiguous inputs that would be hard to classify at the patch scale, even by a human expert. The most common causes of miss-classification are: (i) ambiguous labeling (a fading line or a line annotation near the detection area), (ii) annotation error (inaccuracy position or human mistake), and (iii) strong noise at the patch location. The proportion of ambiguous patches varies between datasets, which explains why the average line classification accuracy differs. Transition lines from GaAs-QD and Si-OG-QD can be irregular and fading (respectively 94.4% and 92.5% accuracy with best models), while Si-SG-QD lines are straight and more predictable, simplifying patches classification (96.9% accuracy with CNN). The most challenging errors to address are the ones related to out-of-distribution issues caused by features in the test diagram that were missing from the training set. In an online scenario, this issue could occur if the device we are trying to tune is too different or present physical defects that were not existing in the previous experiments. This problem could be mitigated by a more diversified training set, a higher QD fabrication quality with less variability, or a reliable confidence score that correctly expresses the distributional uncertainty.

One can improve the effective model accuracy by excluding the model predictions below the confidence threshold. The model outputs can then be interpreted as a three-class inference: “*line*” (output = 1 and confidence  $\geq$  threshold), “*no-line*” (output = 0 and confidence  $\geq$  threshold), and “*unknown*” (confidence < threshold). On average across all datasets and models, this approach decreases the number of errors by 70%, at the price of 11% of patches classified as “*unknown*” (Table 1 and supplementary Figure S7). This method pushes the CNN classification accuracy above 97% for every dataset, which opens the way to robust autotuning procedures. However, we did not observe a benefit of using the Bayesian confidence score compared to the classical heuristic.

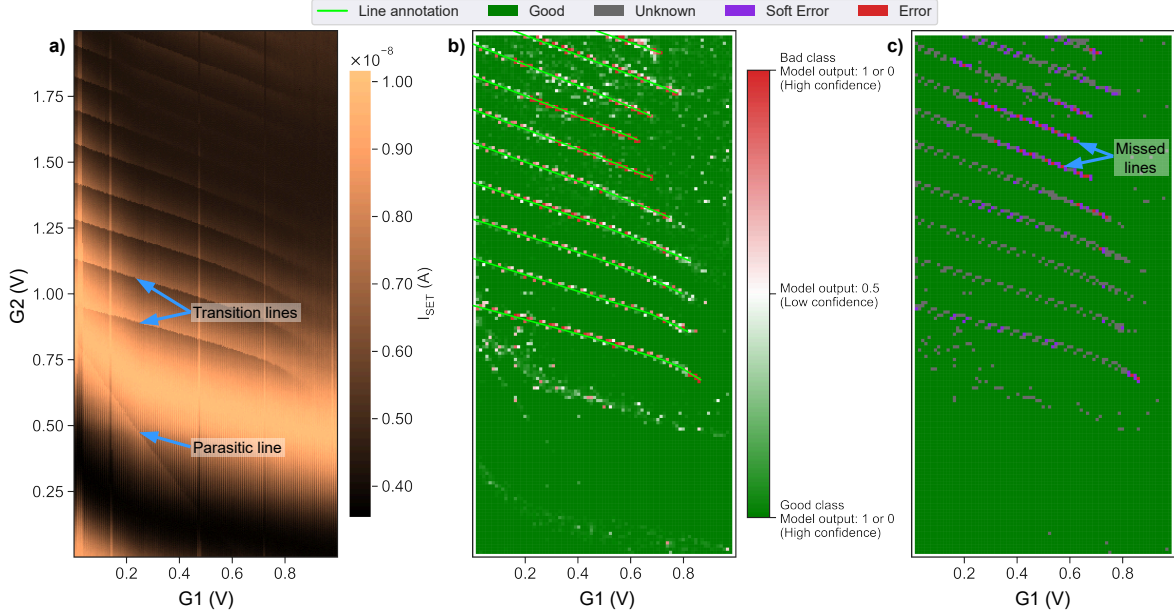


Figure 4: (a) Example of a stability diagram from the Si-OG-QD dataset. This specific diagram presents a parasitic line in the low-voltage area. (b) The same stability diagram is divided into patches classified with a CNN trained using cross-validation [62] (supplementary Figure S4). The color gradient of the patches represents the model uncertainty, where 0.5 is the lowest confidence score according to the Formula 1. The confidence score is lower in low-contrast areas, around the parasitic line, and near transition lines (due to possible intersection ambiguity between the line labels and the detection area of the patch). (c) The same stability diagram after the application of the confidence threshold. Most errors are avoided, except for the end of a few fading lines and some line sections in the low current area at the top of the diagram. The “soft errors” represent misclassifications near a line, which is not expected to induce a tuning error.

Dataset	Model	Accuracy	Accuracy above threshold	Error reduction using threshold	Rate below threshold
Si-SG-QD	BCNN	96.9% $\pm$ 0.1	99.3% $\pm$ 0.1	78.8% $\pm$ 3.0	4.8% $\pm$ 0.4
	CNN	96.9% $\pm$ 0.1	<b>99.4%</b> $\pm$ 0.1	82.4% $\pm$ 2.7	4.9% $\pm$ 0.5
	FF	90.4% $\pm$ 1.1	99.3% $\pm$ 0.1	90.8% $\pm$ 1.3	22.3% $\pm$ 1.3
GaAs-QD	BCNN	93.3% $\pm$ 0.5	96.2% $\pm$ 0.4	48.5% $\pm$ 6.8	9.5% $\pm$ 1.1
	CNN	94.6% $\pm$ 0.2	<b>97.4%</b> $\pm$ 0.2	59.6% $\pm$ 4.3	8.4% $\pm$ 0.8
	FF	93.1% $\pm$ 0.2	96.5% $\pm$ 0.4	57.5% $\pm$ 5.9	9.4% $\pm$ 1.6
Si-OG-QD	BCNN	92.5% $\pm$ 0.4	96.9% $\pm$ 0.3	56.8% $\pm$ 3.2	10.6% $\pm$ 0.7
	CNN	90.7% $\pm$ 0.3	<b>98.1%</b> $\pm$ 0.2	77.8% $\pm$ 1.9	16.2% $\pm$ 0.5
	FF	90.8% $\pm$ 0.2	97.9% $\pm$ 0.1	77.8% $\pm$ 1.0	17.0% $\pm$ 0.5

Table 1: Line detection results for each dataset and model. The performances are averaged over 10 runs with different random seeds. The standard deviation of the runs’ performances represents the variability of the methods. Each run is a cross-validation over every diagram of the dataset. The best test accuracy scores of each dataset are highlighted in bold. The equivalent table without cross-validation is available in supplementary Table S4.

## 4 Autotuning

### 4.1 Method

Now that we have established a high-accuracy line detection method with NNs, we need to define an exploration strategy that uses the model classification and uncertainty to efficiently explore the stability diagram space until the region of interest can be located. One step of this exploration is a cycle of: (i) patch measurement from a charge sensor on the device (simulated by extracting data from offline diagrams in this study), (ii) line detection with the trained NN, and (iii) deciding the following patch coordinates based on the exploration policy. The borders of the diagrams constrain



the exploration to safe gate voltage ranges. The number of steps can be seen as a proxy of the relative tuning time since the measurement is the longest part of the tuning process by orders of magnitude. The actual duration depends on the number of data points, the sensor type, and the electronic performance. For example, obtaining a  $18 \times 18$  patch of Si-SG-QD takes around 2 min by measuring the SET current for the 324 points over a range of  $36 \times 36$  mV with a *Keysight 34465A* multimeter. Although the measurement time can be shortened with more advanced and integrated equipment, it is likely to remain the limiting factor. Therefore, our exploration strategy aims to minimize the number of steps while maximizing the tuning success rate.

The typical strategy [22, 23, 26, 37] is to first search for the zero-electron regime, which is characterized by the absence of transition lines in a large area (bottom left corners in Figure 2 diagrams). Then, we count the number of transition lines until we reach the desired regime. In the case of one-electron tuning, the target location will be between the first and second lines. But such a simple exploration strategy is very fragile to misclassification or hardware changes.

To make the exploration robust and compatible with most QD technologies, we adapt this exploration strategy as illustrated in the Figure 5 and the video<sup>2</sup>. This approach can adapt on the fly to different line slopes (step 2) and spacing (step 3) while checking eventual fading lines (step 4). When a patch is classified with a confidence score below the threshold, we explore the neighboring space around it to reduce the risk of critical failure due to NN misclassification. We validate or refute the presence of a line with additional steps in its supposed direction (see purple arrow in Figure 5b step 4) until a patch is classified with high confidence.

We evaluated this exploration strategy for each diagram that contains the one-electron regime within the measured voltage range (9 for each dataset). We used a k-fold cross-validation method [62] (supplementary Figure S4) to test our approach on every valid diagram, while preventing the inclusion of testing patches in the training set. This testing method should be close to an online autotuning situation, where we want to tune a new device based on previous experiments. The tuning success represents the proportion of final voltage coordinates inside the one-electron regime area, over 50 random starting points for every diagram of the dataset. The whole experiment is reproduced 10 times with different random seeds that affect the NN parameters initialization, the training process, and the random starting points. In total,  $1.1 \times 10^7$  steps have been evaluated in 81,000 offline autotuning simulations with 810 independently trained NNs.

## 4.2 Results

The experiment results for each possible combination of dataset and NN are summarized in Table 2, with the autotuning success rate using, or not, the NN’s confidence score (uncertainty-based). Using the model uncertainty information consistently reduces the number of tuning failures ( $-53\%$  on average) at the price of a few additional steps ( $+22\%$  on average). The best improvement is observed with CNN on Si-SG-QD, where the tuning success rate increased from  $88.8\%$  to  $99.5\%$  when the autotuning procedure exploits the confidence score ( $-95\%$  tuning failures and  $+8.5\%$  steps).

Surprisingly, the confidence score provided by the Bayesian version of the CNN does not provide a significant improvement over the simple heuristic obtained by the standard CNN. The average line detection accuracy is similar for CNN and BCNN on the Si-SG-QD dataset, and the line detection performance is slightly better with BCNN on Si-OG-QD. However, on every dataset, the CNN reaches the higher tuning success using the confidence heuristic score (highlighted in bold in Table 2). Even in the case where the BCNN line detection accuracy is higher (Si-OG-QD), the tuning success benefits more from the CNN confidence score ( $+16.4\%$  tuning success) than the one from BCNN ( $+8.9\%$  tuning success). This result suggests that the number of critical misclassifications above the confidence threshold is more frequent with the Bayesian NN’s uncertainty than with the classical confidence heuristic score.

The line detection accuracy can give valuable indications on the NN performance, but it is not entirely correlated to the tuning success rate since some misclassifications are much more harmful than others during the diagram exploration. If a classification error occurs near a line (soft errors in Figure 4c), it will likely be corrected at the next step. However, an error on a line, or far from it, will probably affect the final tuning result. For example, if a noisy patch is wrongly classified as a line in the empty regime area, the number of charge carriers inside the QD will be overestimated by one.

The uncertainty-based autotuning method with convolution models allows a nearly perfect tuning success rate ( $>99\%$ ) on the Si-SG-QD dataset. This high performance is attributable to (i) the convolution layers’ capability to efficiently filter the oscillating background noise, (ii) the exploitation of the model confidence score to prevent most critical errors, and (iii) the straight transition lines that simplify the exploration. The line detection task also benefits from the large training set (72,000 patches) and the low variability between diagram features.

<sup>2</sup>Method presentation and animated autotuning examples: <https://youtu.be/9pPrgrIx900>

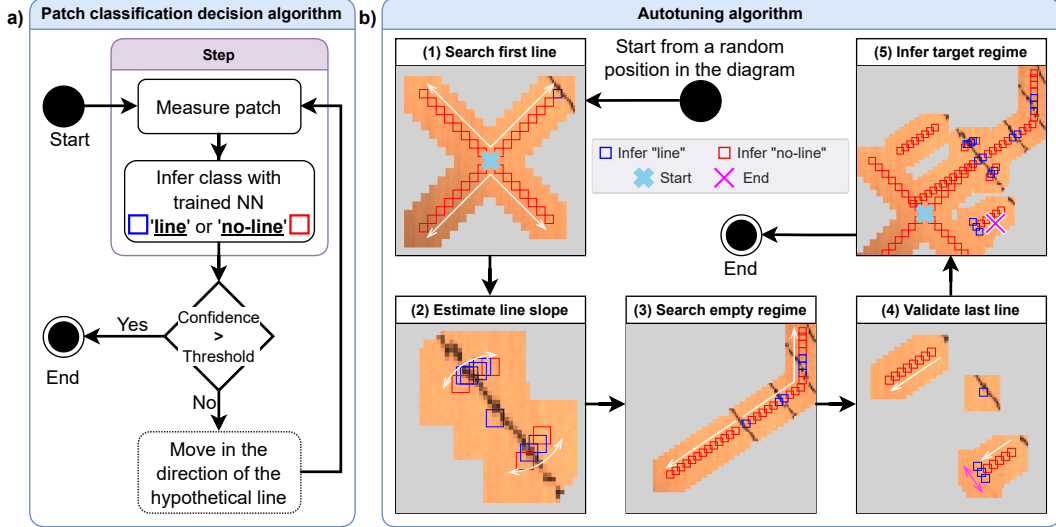


Figure 5: **(a)** Schematic representation of the patch classification algorithm. The purple box wraps the logic of one exploration step. **(b)** Step-by-step example of the autotuning algorithm using GaAs-QD dataset (complete diagram in Figure 2b). The arrows represent the direction of the exploration, and the gray area is unmeasured space during the current step. (1) Search the first line by exploring the voltage space in 4 directions. (2) Estimate the line slope by scanning two sequences of patches in circular arcs around the first patch with a line. (3) Explore space perpendicularly to the first line to gather information about the distance between lines. Stop after reaching 3 times the average distance without detecting a new line in lower voltages. (4) Search for possible missed lines under the first line by scanning multiple sections where we would expect to find a new line according to average line distance and slope estimation. In this example, a fading line is correctly detected at the bottom of the image, but the low confidence of the model triggers a validation procedure. More scans are then processed on the hypothetical line direction (purple arrow) until a higher confidence inference validates or invalidates the line’s existence. (5) Deduce the one-electron regime location based on the leftmost line position, the slope, and the average space between lines (all scans from previous steps are represented here). The algorithmic detail of each step is available in supplementary Section S3.1.

The GaAs-QD and Si-OG-QD datasets present more diversity of features in their diagram with a smaller training set, which makes the classification task more challenging. The shape of the transition lines is also less predictable than the Si-SG-QD dataset, which increases the risk of missing a line or failing to detect its slope and spacing. The significantly higher tuning performance without cross-validation (supplementary Table S5) suggests that the training sets do not cover the diversity of stability diagrams. Which is well illustrated by CNNs on GaAs-QD, where the tuning success rate is improved by 11.6 % without cross-validation (92.2 % against 80.6 %). This hypothesis is confirmed by the high variability of tuning success rates between diagrams in these two datasets. The results are very polarized between the diagrams for which the one-electron regime is found nearly 100 % of the time, and some are more complex to tune with a very low success rate. A larger or more consistent dataset could reduce the tuning success loss observed with cross-validation.

Overall, noise and hardware imperfections are relatively easy to manage for the line detection task but more challenging to deal with at the diagram scale during exploration. Therefore, the reliability of an autotuning procedure is mainly affected by the shape and consistency of the transition lines.

Dataset	Model	Line detection accuracy	Uncertainty-based tuning	Average step number	Tuning success
Si-SG-QD	BCNN	96.9% $\pm 0.1$	Yes	164	99.2% $\pm 0.7$
			No	148	88.2% $\pm 2.3$
	CNN	96.9% $\pm 0.1$	Yes	165	<b>99.5%</b> $\pm 0.7$
			No	152	88.8% $\pm 2.4$
	FF	90.4% $\pm 1.1$	Yes	194	72.4% $\pm 6.3$
			No	122	23.9% $\pm 5.4$
GaAs-QD	BCNN	93.3% $\pm 0.5$	Yes	104	75.3% $\pm 4.2$
			No	92	55.9% $\pm 3.8$
	CNN	94.6% $\pm 0.2$	Yes	103	<b>80.6%</b> $\pm 3.9$
			No	93	72.4% $\pm 2.9$
	FF	93.1% $\pm 0.2$	Yes	105	72.8% $\pm 4.5$
			No	92	58.4% $\pm 3.4$
Si-OG-QD	BCNN	92.5% $\pm 0.4$	Yes	185	75.2% $\pm 2.5$
			No	155	66.3% $\pm 3.4$
	CNN	90.7% $\pm 0.3$	Yes	193	<b>78.1%</b> $\pm 1.7$
			No	150	61.7% $\pm 3.0$
	FF	90.8% $\pm 0.2$	Yes	200	78.0% $\pm 2.5$
			No	151	59.3% $\pm 2.4$

Table 2: Autotuning results for each dataset and model, with and without using the model uncertainty information provided by the confidence score. The line detection accuracy and tuning success variability are computed over 10 runs with different random seeds. Each run is a cross-validation over every diagram of the dataset. The best tuning success rates of each dataset are highlighted in bold. The tuning success rates can be compared to the baselines presented in supplementary Table S3. The equivalent table without cross-validation is available in supplementary Table S5.

## 5 Discussion

The proposed method can be used to automate the charge tuning of any spin-based semiconductor single QD, with less than 10 annotated stability diagrams for training and some basic prior knowledge of the device characteristics (expected working range voltage, approximate transition lines slope, and spacing). The autotuning procedure is resilient to noise and physical imperfections but sensitive to high device-to-device variability and the training dataset quality (number of diagrams and features coverage). This is well illustrated by the Si-SG-QD dataset, which features strong noise but consistent diagrams, allowing a robust autotuning procedure with only 23 tuning failures over 4500 CNN uncertainty-based tuning simulations. Therefore, this method, associated with good fabrication yield, has the potential to enable parallel charge tuning of large QD arrays, which is currently not practical with a manual approach.

This study shows the benefit of using NN uncertainty to automate the tuning of QDs with only partial measurement of the stability diagrams. The confidence score provides valuable information about the model prediction, which can be used to design robust autotuning procedures. However, we did not see a clear benefit of using a Bayesian NN over the standard one, even though Bayesian models are specifically designed to provide uncertainty measurement. This behavior could be explained by the distributional uncertainty poorly captured by the Bayesian NNs [63], which could be the predominant source of uncertainty with the cross-validation testing method. Moreover, many approximations [27] are necessary to keep the Bayesian NN training and inference tractable, which could be detrimental to the overall quality of the model and its coherence with the initial Bayesian framework. Thus, the additional complexity and computing cost induced by Bayesian NN is hard to justify, while a simpler NN can provide a more reliable confidence score. In future works, other methods of uncertainty quantification [64] could be evaluated to improve the confidence score reliability (e.g., dropout as Bayesian approximation [28] or ensemble learning [65]). Bayesian optimization associated with classical machine learning [66, 67] also appears to be a promising avenue to harness the complexity of quantum engineering.

While applying quantum computing gates requires more than one QD, we developed and tested our approach on single QD datasets as a first step toward robust double and triple QD autotuning. Since NNs are known for their good scalability, we expect this method to be expandable to larger input dimensions [34, 68] and greater numbers of classes. When the problem’s complexity increases, the benefit of the confidence score could become even more important.

To avoid any wiring bottleneck [69] between the fridge and external electronics, such a calibration method could be integrated near the QDs, in the 4 K stage of the cryogenic environment. One way to meet this requirement would be to transfer the trained NN on low-power and cryo-compatible hardware, such as circuits based on arrays of memristive

devices [70–72]. This specialized hardware takes advantage of in-memory computing [73, 74] to efficiently perform the multiply-accumulate operations [75] required by NN inference. Therefore, memristor-based systems represent promising candidates to realize scalable autotuning from inside the fridge with close-loop measurement and minimal disturbance over the QDs. Future works should be done to simulate such hardware implementations and demonstrate real time online autotuning with the proposed method.

## Acknowledgments

VY acknowledges Stefanie Czischek who inspired this study by working on a first version of the autotuning procedure. And every experimentalist who provides the stability diagram measurements used in this paper (Michel Pioro-Ladrière, Marc-Antoine Roux, Marc-Antoine Genest, Julien Camirand-Lemire, and Sophie Rochette).

VY, BG, YB, and DD acknowledge support from the National Science Engineering Research Council of Canada Grant ALLRP 580722 – 22 et Fond Recherche Québec Nature et Technologies Grant 300253

RGM acknowledges support from NSERC and the Perimeter Institute for Theoretical Physics. Research at Perimeter Institute is supported in part by the Government of Canada through the Department of Innovation, Science and Economic Development Canada and by the Province of Ontario through the Ministry of Economic Development, Job Creation and Trade.

## Conflict of interest

The authors have no conflicts to disclose.

## Author contributions

All authors contributed to the article and approved the submitted version.

Victor Yon: methodology, datasets aggregation and processing, software implementation, run experiments, results analysis and visualization, writing original draft

Bastien Galaup: contributes to software implementation and running experiments, review and editing

Claude Rohrbacher and Joffrey Rivard: provide data for Si-OG-QD dataset, provide expertise and technical assistance on quantum dot technology, review and editing

Clément Godfrin, Roy Li, Stefan Kubicek, and Kristiaan De Greve: Manufactured the devices used to obtain the Si-OG-QD dataset

Louis Gaudreau: provides data for GaAs-QD dataset, provides expertise and technical assistance on quantum dot technology, review and editing

Yann Beilliard: methodology, supervision, funding acquisition, review and editing

Eva Dupont-Ferrier and Roger Melko: supervision, review and editing

Dominique Drouin: methodology, supervision, funding acquisition, review and editing

## Code and data availability

The python code source used to aggregate and build the quantum dot stability diagrams dataset is publicly accessible on *GitHub*: <https://github.com/3it-inpaqt/qdsd-dataset>.

The python code source used to run all the experiments presented in this article is publicly accessible on *GitHub*: <https://github.com/3it-inpaqt/dot-calibration-v2/tree/offline-article>.

Raw and processed stability diagram measurements used to train and test the model presented in the article are publicly available for downloading from Yon et al. [43].

All simulation outputs and results used to generate the tables and figures presented in this article are publicly available for downloading from Yon et al. [76].

## References

- [1] Daniel Loss and David P. DiVincenzo. Quantum computation with quantum dots. *Physical Review A*, 57(1): 120–126, January 1998. ISSN 1094-1622. doi:10.1103/physreva.57.120. URL <http://dx.doi.org/10.1103/PhysRevA.57.120>.
- [2] M. Veldhorst, C. H. Yang, J. C. C. Hwang, W. Huang, J. P. Dehollain, J. T. Muhonen, S. Simmons, A. Laucht, F. E. Hudson, K. M. Itoh, A. Morello, and A. S. Dzurak. A two-qubit logic gate in silicon. *Nature*, 526(7573): 410–414, October 2015. ISSN 1476-4687. doi:10.1038/nature15263. URL <http://dx.doi.org/10.1038/nature15263>.
- [3] T. F. Watson, S. G. J. Philips, E. Kawakami, D. R. Ward, P. Scarlino, M. Veldhorst, D. E. Savage, M. G. Lagally, Mark Friesen, S. N. Coppersmith, M. A. Eriksson, and L. M. K. Vandersypen. A programmable two-qubit quantum processor in silicon. *Nature*, 555(7698):633–637, February 2018. ISSN 1476-4687. doi:10.1038/nature25766. URL <http://dx.doi.org/10.1038/nature25766>.
- [4] Guido Burkard, Thaddeus D. Ladd, Andrew Pan, John M. Nichol, and Jason R. Petta. Semiconductor spin qubits. *Reviews of Modern Physics*, 95(2), June 2023. ISSN 1539-0756. doi:10.1103/revmodphys.95.025003. URL <http://dx.doi.org/10.1103/RevModPhys.95.025003>.
- [5] Kenta Takeda, Jun Kamioka, Tomohiro Otsuka, Jun Yoneda, Takashi Nakajima, Matthieu R. Delbecq, Shinichi Amaha, Giles Allison, Tetsuo Kodera, Shunri Oda, and Seigo Tarucha. A fault-tolerant addressable spin qubit in a natural silicon quantum dot. *Science Advances*, 2(8), August 2016. ISSN 2375-2548. doi:10.1126/sciadv.1600694. URL <http://dx.doi.org/10.1126/sciadv.1600694>.
- [6] Jun Yoneda, Kenta Takeda, Tomohiro Otsuka, Takashi Nakajima, Matthieu R. Delbecq, Giles Allison, Takumu Honda, Tetsuo Kodera, Shunri Oda, Yusuke Hoshi, Noritaka Usami, Kohei M. Itoh, and Seigo Tarucha. A quantum-dot spin qubit with coherence limited by charge noise and fidelity higher than 99.9%. *Nature Nanotechnology*, 13(2): 102–106, December 2017. ISSN 1748-3395. doi:10.1038/s41565-017-0014-x. URL <http://dx.doi.org/10.1038/s41565-017-0014-x>.
- [7] Adam R. Mills, Charles R. Guinn, Michael J. Gullans, Anthony J. Sigillito, Mayer M. Feldman, Erik Nielsen, and Jason R. Petta. Two-qubit silicon quantum processor with operation fidelity exceeding 99%. *Science Advances*, 8(14), April 2022. ISSN 2375-2548. doi:10.1126/sciadv.abn5130. URL <http://dx.doi.org/10.1126/sciadv.abn5130>.
- [8] Akito Noiri, Kenta Takeda, Takashi Nakajima, Takashi Kobayashi, Amir Sammak, Giordano Scappucci, and Seigo Tarucha. A shuttling-based two-qubit logic gate for linking distant silicon quantum processors. *Nature Communications*, 13(1), September 2022. ISSN 2041-1723. doi:10.1038/s41467-022-33453-z. URL <http://dx.doi.org/10.1038/s41467-022-33453-z>.
- [9] Xiao Xue, Maximilian Russ, Nodar Samkharadze, Brennan Undseth, Amir Sammak, Giordano Scappucci, and Lieven M. K. Vandersypen. Quantum logic with spin qubits crossing the surface code threshold. *Nature*, 601(7893):343–347, January 2022. ISSN 1476-4687. doi:10.1038/s41586-021-04273-w. URL <http://dx.doi.org/10.1038/s41586-021-04273-w>.
- [10] Alexei M. Tyryshkin, Shinichi Tojo, John J. L. Morton, Helge Riemann, Nikolai V. Abrosimov, Peter Becker, Hans-Joachim Pohl, Thomas Schenkel, Michael L. W. Thewalt, Kohei M. Itoh, and S. A. Lyon. Electron spin coherence exceeding seconds in high-purity silicon. *Nature Materials*, 11(2):143–147, December 2011. ISSN 1476-4660. doi:10.1038/nmat3182. URL <http://dx.doi.org/10.1038/nmat3182>.
- [11] M. Veldhorst, J. C. C. Hwang, C. H. Yang, A. W. Leenstra, B. de Ronde, J. P. Dehollain, J. T. Muhonen, F. E. Hudson, K. M. Itoh, A. Morello, and A. S. Dzurak. An addressable quantum dot qubit with fault-tolerant control-fidelity. *Nature Nanotechnology*, 9(12):981–985, October 2014. ISSN 1748-3395. doi:10.1038/nnano.2014.216. URL <http://dx.doi.org/10.1038/nnano.2014.216>.
- [12] Luca Petit, Maximilian Russ, Gertjan H. G. J. Eenink, William I. L. Lawrie, James S. Clarke, Lieven M. K. Vandersypen, and Menno Veldhorst. Design and integration of single-qubit rotations and two-qubit gates in silicon above one kelvin. *Communications Materials*, 3(1), November 2022. ISSN 2662-4443. doi:10.1038/s43246-022-00304-9. URL <http://dx.doi.org/10.1038/s43246-022-00304-9>.
- [13] R. Maurand, X. Jehl, D. Kotekar-Patil, A. Corna, H. Bohuslavskiy, R. Laviéville, L. Hutin, S. Barraud, M. Vinet, M. Sanquer, and S. De Franceschi. A cmos silicon spin qubit. *Nature Communications*, 7(1), November 2016. ISSN 2041-1723. doi:10.1038/ncomms13575. URL <http://dx.doi.org/10.1038/ncomms13575>.
- [14] N. I. Dumoulin Stuyck, R. Li, C. Godfrin, A. Elsayed, S. Kubicek, J. Jussot, B. T. Chan, F. A. Mohiyaddin, M. Shehata, G. Simion, Y. Canvel, L. Goux, M. Heyns, B. Govoreanu, and I. P. Radu. Uniform spin qubit

- devices with tunable coupling in an all-silicon 300 nm integrated process. In *2021 Symposium on VLSI Circuits*. IEEE, June 2021. doi:10.23919/vlsicircuits52068.2021.9492427. URL <http://dx.doi.org/10.23919/VLSICircuits52068.2021.9492427>.
- [15] M. F. Gonzalez-Zalba, S. de Franceschi, E. Charbon, T. Meunier, M. Vinet, and A. S. Dzurak. Scaling silicon-based quantum computing using cmos technology. *Nature Electronics*, 4(12):872–884, December 2021. ISSN 2520-1131. doi:10.1038/s41928-021-00681-y. URL <http://dx.doi.org/10.1038/s41928-021-00681-y>.
- [16] C. Rohrbacher, J. Rivard, R. Ritzenthaler, B. Bureau, C. Lupien, H. Mertens, N. Horiguchi, and E. Dupont-Ferrier. Dual operation of gate-all-around silicon nanowires at cryogenic temperatures: Fet and quantum dot, 2023. URL <https://arxiv.org/abs/2312.00903>.
- [17] Xiaolong Liu and Mark C. Hersam. 2d materials for quantum information science. *Nature Reviews Materials*, 4(10):669–684, August 2019. ISSN 2058-8437. doi:10.1038/s41578-019-0136-x. URL <http://dx.doi.org/10.1038/s41578-019-0136-x>.
- [18] Andre Saraiva, Wee Han Lim, Chih Hwan Yang, Christopher C. Escott, Arne Laucht, and Andrew S. Dzurak. Materials for silicon quantum dots and their impact on electron spin qubits. *Advanced Functional Materials*, 32(3), December 2021. ISSN 1616-3028. doi:10.1002/adfm.202105488. URL <http://dx.doi.org/10.1002/adfm.202105488>.
- [19] Rashmit Patel, Yash Agrawal, and Rutu Parekh. Single-electron transistor: review in perspective of theory, modelling, design and fabrication. *Microsystem Technologies*, 27(5):1863–1875, September 2020. ISSN 1432-1858. doi:10.1007/s00542-020-05002-5. URL <http://dx.doi.org/10.1007/s00542-020-05002-5>.
- [20] C. B. Simmons, Madhu Thalakulam, Nakul Shaji, Levente J. Klein, Hua Qin, R. H. Blick, D. E. Savage, M. G. Lagally, S. N. Coppersmith, and M. A. Eriksson. Single-electron quantum dot in si/sige with integrated charge sensing. *Applied Physics Letters*, 91(21), November 2007. ISSN 1077-3118. doi:10.1063/1.2816331. URL <http://dx.doi.org/10.1063/1.2816331>.
- [21] T. A. Baart, P. T. Eendebak, C. Reichl, W. Wegscheider, and L. M. K. Vandersypen. Computer-automated tuning of semiconductor double quantum dots into the single-electron regime. *Applied Physics Letters*, 108(21), May 2016. ISSN 1077-3118. doi:10.1063/1.4952624. URL <http://dx.doi.org/10.1063/1.4952624>.
- [22] Stefanie Czischek, Victor Yon, Marc-Antoine Genest, Marc-Antoine Roux, Sophie Rochette, Julien Camirand Lemyre, Mathieu Moras, Michel Pioro-Ladrière, Dominique Drouin, Yann Beilliard, and Roger G Melko. Miniaturizing neural networks for charge state autotuning in quantum dots. *Machine Learning: Science and Technology*, 3(1):015001, November 2021. ISSN 2632-2153. doi:10.1088/2632-2153/ac34db. URL <http://dx.doi.org/10.1088/2632-2153/ac34db>.
- [23] R. Durrer, B. Kratochwil, J.V. Koski, A.J. Landig, C. Reichl, W. Wegscheider, T. Ihn, and E. Greplova. Automated tuning of double quantum dots into specific charge states using neural networks. *Physical Review Applied*, 13(5), May 2020. ISSN 2331-7019. doi:10.1103/physrevapplied.13.054019. URL <http://dx.doi.org/10.1103/PhysRevApplied.13.054019>.
- [24] Yann LeCun, Yoshua Bengio, and Geoffrey Hinton. Deep learning. *Nature*, 521(7553):436–444, May 2015. ISSN 1476-4687. doi:10.1038/nature14539. URL <http://dx.doi.org/10.1038/nature14539>.
- [25] Joshua Ziegler, Thomas McJunkin, E.S. Joseph, Sandesh S. Kalantre, Benjamin Harpt, D.E. Savage, M.G. Lagally, M.A. Eriksson, Jacob M. Taylor, and Justyna P. Zwolak. Toward robust autotuning of noisy quantum dot devices. *Physical Review Applied*, 17(2), February 2022. ISSN 2331-7019. doi:10.1103/physrevapplied.17.024069. URL <http://dx.doi.org/10.1103/PhysRevApplied.17.024069>.
- [26] Joshua Ziegler, Florian Luthi, Mick Ramsey, Felix Borjans, Guoji Zheng, and Justyna P. Zwolak. Tuning arrays with rays: Physics-informed tuning of quantum dot charge states. *Physical Review Applied*, 20(3), September 2023. ISSN 2331-7019. doi:10.1103/physrevapplied.20.034067. URL <http://dx.doi.org/10.1103/PhysRevApplied.20.034067>.
- [27] Ethan Goan and Clinton Fookes. *Bayesian Neural Networks: An Introduction and Survey*, page 45–87. Springer International Publishing, 2020. ISBN 9783030425531. doi:10.1007/978-3-030-42553-1\_3. URL [http://dx.doi.org/10.1007/978-3-030-42553-1\\_3](http://dx.doi.org/10.1007/978-3-030-42553-1_3).
- [28] Yarin Gal. *Uncertainty in Deep Learning*. PhD thesis, University of Cambridge, 2016.
- [29] Hanwei Liu, Baochuan Wang, Ning Wang, Zhonghai Sun, Huili Yin, Haiou Li, Gang Cao, and Guoping Guo. An automated approach for consecutive tuning of quantum dot arrays. *Applied Physics Letters*, 121(8), August 2022. ISSN 1077-3118. doi:10.1063/5.0111128. URL <http://dx.doi.org/10.1063/5.0111128>.



- [30] Justyna P. Zwolak, Thomas McJunkin, Sandesh S. Kalantre, J.P. Dodson, E.R. MacQuarrie, D.E. Savage, M.G. Lagally, S.N. Coppersmith, Mark A. Eriksson, and Jacob M. Taylor. Autotuning of double-dot devices in situ with machine learning. *Physical Review Applied*, 13(3), March 2020. ISSN 2331-7019. doi:10.1103/physrevapplied.13.034075. URL <http://dx.doi.org/10.1103/PhysRevApplied.13.034075>.
- [31] B. Severin, D. T. Lennon, L. C. Camenzind, F. Vigneau, F. Fedele, D. Jirovec, A. Ballabio, D. Chrastina, G. Isella, M. de Kruijff, M. J. Carballido, S. Svab, A. V. Kuhlmann, F. R. Braakman, S. Geyer, F. N. M. Froning, H. Moon, M. A. Osborne, D. Sejdinovic, G. Katsaros, D. M. Zumbühl, G. A. D. Briggs, and N. Ares. Cross-architecture tuning of silicon and sige-based quantum devices using machine learning, 2021. URL <https://arxiv.org/abs/2107.12975>.
- [32] Sandesh S. Kalantre, Justyna P. Zwolak, Stephen Ragole, Xingyao Wu, Neil M. Zimmerman, M. D. Stewart, and Jacob M. Taylor. Machine learning techniques for state recognition and auto-tuning in quantum dots. *npj Quantum Information*, 5(1), January 2019. ISSN 2056-6387. doi:10.1038/s41534-018-0118-7. URL <http://dx.doi.org/10.1038/s41534-018-0118-7>.
- [33] J Darulová, M Troyer, and M C Cassidy. Evaluation of synthetic and experimental training data in supervised machine learning applied to charge-state detection of quantum dots. *Machine Learning: Science and Technology*, 2(4):045023, September 2021. ISSN 2632-2153. doi:10.1088/2632-2153/ac104c. URL <http://dx.doi.org/10.1088/2632-2153/ac104c>.
- [34] H. Moon, D. T. Lennon, J. Kirkpatrick, N. M. van Esbroeck, L. C. Camenzind, Liuqi Yu, F. Vigneau, D. M. Zumbühl, G. A. D. Briggs, M. A. Osborne, D. Sejdinovic, E. A. Laird, and N. Ares. Machine learning enables completely automatic tuning of a quantum device faster than human experts. *Nature Communications*, 11(1), August 2020. ISSN 2041-1723. doi:10.1038/s41467-020-17835-9. URL <http://dx.doi.org/10.1038/s41467-020-17835-9>.
- [35] Justin K Perron, M D Stewart Jr, and Neil M Zimmerman. A quantitative study of bias triangles presented in chemical potential space. *Journal of Physics: Condensed Matter*, 27(23):235302, May 2015. ISSN 1361-648X. doi:10.1088/0953-8984/27/23/235302. URL <http://dx.doi.org/10.1088/0953-8984/27/23/235302>.
- [36] Toivo Hensgens. *Emulating Fermi-Hubbard physics with quantum dots*. Phd thesis, Delft University of Technology, 2018. URL <http://resolver.tudelft.nl/uuid:b71f3b0b-73a0-4996-896c-84ed43e72035>.
- [37] M. Lapointe-Major, O. Germain, J. Camirand Lemyre, D. Lachance-Quirion, S. Rochette, F. Camirand Lemyre, and M. Pioro-Ladrière. Algorithm for automated tuning of a quantum dot into the single-electron regime. *Physical Review B*, 102(8), August 2020. ISSN 2469-9969. doi:10.1103/physrevb.102.085301. URL <http://dx.doi.org/10.1103/PhysRevB.102.085301>.
- [38] Julian D. Teske, Simon Sebastian Humpohl, René Otten, Patrick Bethke, Pascal Cerfontaine, Jonas Dedden, Arne Ludwig, Andreas D. Wieck, and Hendrik Bluhm. A machine learning approach for automated fine-tuning of semiconductor spin qubits. *Applied Physics Letters*, 114(13), April 2019. ISSN 1077-3118. doi:10.1063/1.5088412. URL <http://dx.doi.org/10.1063/1.5088412>.
- [39] Justyna P. Zwolak and Jacob M. Taylor. Colloquium : Advances in automation of quantum dot devices control. *Reviews of Modern Physics*, 95(1), February 2023. ISSN 1539-0756. doi:10.1103/revmodphys.95.011006. URL <http://dx.doi.org/10.1103/RevModPhys.95.011006>.
- [40] S. Rochette, M. Rudolph, A.-M. Roy, M. J. Curry, G. A. Ten Eyck, R. P. Manginell, J. R. Wendt, T. Pluym, S. M. Carr, D. R. Ward, M. P. Lilly, M. S. Carroll, and M. Pioro-Ladrière. Quantum dots with split enhancement gate tunnel barrier control. *Applied Physics Letters*, 114(8), February 2019. ISSN 1077-3118. doi:10.1063/1.5091111. URL <http://dx.doi.org/10.1063/1.5091111>.
- [41] L. Gaudreau, A. Kam, G. Granger, S. A. Studenikin, P. Zawadzki, and A. S. Sachrajda. A tunable few electron triple quantum dot. *Applied Physics Letters*, 95(19), November 2009. ISSN 1077-3118. doi:10.1063/1.3258663. URL <http://dx.doi.org/10.1063/1.3258663>.
- [42] Justyna P. Zwolak, Sandesh S. Kalantre, Xingyao Wu, Stephen Ragole, and Jacob M. Taylor. Qflow lite dataset: A machine-learning approach to the charge states in quantum dot experiments. *PLOS ONE*, 13(10):e0205844, October 2018. ISSN 1932-6203. doi:10.1371/journal.pone.0205844. URL <http://dx.doi.org/10.1371/journal.pone.0205844>.
- [43] Victor Yon, Bastien Galaup, Marc-Antoine Roux, Marc-Antoine Genest, Claude Rohrbacher, Joffrey Rivard, Clément Godfrin, Roy Li, Kristiaan De Greve, Sophie Rochette, Julien Camirand-Lemire, Louis Gaudreau, Michel Pioro-Ladrière, Yann Beilliard, Roger G. Melko, and Dominique and Drouin. Quantum dots stability diagrams dataset, May 2024. URL <https://doi.org/10.5281/zenodo.11402792>.

- [44] Shervin Minaee, Yuri Y. Boykov, Fatih Porikli, Antonio J Plaza, Nasser Kehtarnavaz, and Demetri Terzopoulos. Image segmentation using deep learning: A survey. *IEEE Transactions on Pattern Analysis and Machine Intelligence*, page 1–1, 2021. ISSN 1939-3539. doi:10.1109/tpami.2021.3059968. URL <http://dx.doi.org/10.1109/TPAMI.2021.3059968>.
- [45] Yichi Zhang, Zhenrong Shen, and Rushi Jiao. Segment anything model for medical image segmentation: Current applications and future directions. *Computers in Biology and Medicine*, 171:108238, March 2024. ISSN 0010-4825. doi:10.1016/j.compbiomed.2024.108238. URL <http://dx.doi.org/10.1016/j.compbiomed.2024.108238>.
- [46] Yoshua Bengio. Deep learning of representations for unsupervised and transfer learning. In Isabelle Guyon, Gideon Dror, Vincent Lemaire, Graham Taylor, and Daniel Silver, editors, *Proceedings of ICML Workshop on Unsupervised and Transfer Learning*, volume 27 of *Proceedings of Machine Learning Research*, pages 17–36, Bellevue, Washington, USA, 02 Jul 2012. PMLR. URL <https://proceedings.mlr.press/v27/bengio12a.html>.
- [47] Leiyu Chen, Shaobo Li, Qiang Bai, Jing Yang, Sanlong Jiang, and Yanming Miao. Review of image classification algorithms based on convolutional neural networks. *Remote Sensing*, 13(22):4712, November 2021. ISSN 2072-4292. doi:10.3390/rs13224712. URL <http://dx.doi.org/10.3390/rs13224712>.
- [48] Benjamin Lienhard, Antti Vepsäläinen, Luke C.G. Govia, Cole R. Hoffer, Jack Y. Qiu, Diego Ristè, Matthew Ware, David Kim, Roni Winik, Alexander Melville, Bethany Niedzielski, Jonilyn Yoder, Guilhem J. Ribeill, Thomas A. Ohki, Hari K. Krovi, Terry P. Orlando, Simon Gustavsson, and William D. Oliver. Deep-neural-network discrimination of multiplexed superconducting-qubit states. *Physical Review Applied*, 17(1), January 2022. ISSN 2331-7019. doi:10.1103/physrevapplied.17.014024. URL <http://dx.doi.org/10.1103/PhysRevApplied.17.014024>.
- [49] Yongchan Kwon, Joong-Ho Won, Beom Joon Kim, and Myunghee Cho Paik. Uncertainty quantification using bayesian neural networks in classification: Application to biomedical image segmentation. *Computational Statistics & Data Analysis*, 142:106816, February 2020. ISSN 0167-9473. doi:10.1016/j.csda.2019.106816. URL <http://dx.doi.org/10.1016/j.csda.2019.106816>.
- [50] Laurent Valentin Jospin, Hamid Laga, Farid Boussaid, Wray Buntine, and Mohammed Bennamoun. Hands-on bayesian neural networks—a tutorial for deep learning users. *IEEE Computational Intelligence Magazine*, 17(2): 29–48, May 2022. ISSN 1556-6048. doi:10.1109/mci.2022.3155327. URL <http://dx.doi.org/10.1109/MCI.2022.3155327>.
- [51] Geoffrey E. Hinton and Drew van Camp. Keeping the neural networks simple by minimizing the description length of the weights. In *Proceedings of the sixth annual conference on Computational learning theory - COLT '93*, COLT '93. ACM Press, 1993. doi:10.1145/168304.168306. URL <http://dx.doi.org/10.1145/168304.168306>.
- [52] Alex Graves. Practical variational inference for neural networks. In J. Shawe-Taylor, R. Zemel, P. Bartlett, F. Pereira, and K.Q. Weinberger, editors, *Advances in Neural Information Processing Systems*, volume 24. Curran Associates, Inc., 2011. URL <https://proceedings.neurips.cc/paper/2011/hash/7eb3c8be3d411e8ebfab08eba5f49632-Abstract.html>.
- [53] Charles Blundell, Julien Cornebise, Koray Kavukcuoglu, and Daan Wierstra. Weight uncertainty in neural networks, 2015. URL <https://arxiv.org/abs/1505.05424>.
- [54] Jakob Gawlikowski, Cedrique Rovile Njiteutcheu Tassi, Mohsin Ali, Jongseok Lee, Matthias Humt, Jianxiang Feng, Anna Kruspe, Rudolph Triebel, Peter Jung, Ribana Roscher, Muhammad Shahzad, Wen Yang, Richard Bamler, and Xiao Xiang Zhu. A survey of uncertainty in deep neural networks, 2021. URL <https://arxiv.org/abs/2107.03342>.
- [55] Lewis Smith and Yarin Gal. Understanding measures of uncertainty for adversarial example detection, 2018. URL <https://arxiv.org/abs/1803.08533>.
- [56] Hugo Zaragoza and Florence d’Alché Buc. Confidence measures for neural network classifiers. In *Proceedings of the Seventh Int. Conf. Information Processing and Management of Uncertainty in Knowledge Based Systems*, volume 9. Citeseer, 1998.
- [57] Amit Mandelbaum and Daphna Weinshall. Distance-based confidence score for neural network classifiers, 2017. URL <https://arxiv.org/abs/1709.09844>.
- [58] Peter Auer. Using confidence bounds for exploitation-exploration trade-offs. *Journal of Machine Learning Research*, 3(Nov):397–422, 2002. URL <https://www.jmlr.org/papers/v3/auer02a.html>.
- [59] Chuan Guo, Geoff Pleiss, Yu Sun, and Kilian Q. Weinberger. On calibration of modern neural networks, 2017. URL <https://arxiv.org/abs/1706.04599>.

- [60] Juozas Vaicenavicius, David Widmann, Carl Andersson, Fredrik Lindsten, Jacob Roll, and Thomas B. Schön. Evaluating model calibration in classification, 2019. URL <https://arxiv.org/abs/1902.06977>.
- [61] Telmo Silva Filho, Hao Song, Miquel Perello-Nieto, Raul Santos-Rodriguez, Meelis Kull, and Peter Flach. Classifier calibration: a survey on how to assess and improve predicted class probabilities. *Machine Learning*, 112(9):3211–3260, May 2023. ISSN 1573-0565. doi:10.1007/s10994-023-06336-7. URL <http://dx.doi.org/10.1007/s10994-023-06336-7>.
- [62] Sebastian Raschka. Model evaluation, model selection, and algorithm selection in machine learning, 2018. URL <https://arxiv.org/abs/1811.12808>.
- [63] Pavel Izmailov, Sharad Vikram, Matthew D Hoffman, and Andrew Gordon Gordon Wilson. What are bayesian neural network posteriors really like? In Marina Meila and Tong Zhang, editors, *Proceedings of the 38th International Conference on Machine Learning*, volume 139 of *Proceedings of Machine Learning Research*, pages 4629–4640. PMLR, 18–24 Jul 2021. URL <https://proceedings.mlr.press/v139/izmailov21a.html>.
- [64] Moloud Abdar, Farhad Pourpanah, Sadiq Hussain, Dana Rezazadegan, Li Liu, Mohammad Ghavamzadeh, Paul Fieguth, Xiaochun Cao, Abbas Khosravi, U. Rajendra Acharya, Vladimir Makarenkov, and Saeid Nahavandi. A review of uncertainty quantification in deep learning: Techniques, applications and challenges. *Information Fusion*, 76:243–297, December 2021. ISSN 1566-2535. doi:10.1016/j.inffus.2021.05.008. URL <http://dx.doi.org/10.1016/j.inffus.2021.05.008>.
- [65] Balaji Lakshminarayanan, Alexander Pritzel, and Charles Blundell. Simple and scalable predictive uncertainty estimation using deep ensembles, 2016. URL <https://arxiv.org/abs/1612.01474>.
- [66] Valentin Gebhart, Raffaele Santagati, Antonio Andrea Gentile, Erik M. Gauger, David Craig, Natalia Ares, Leonardo Banchi, Florian Marquardt, Luca Pezzè, and Cristian Bonato. Learning quantum systems. *Nature Reviews Physics*, 5(3):141–156, February 2023. ISSN 2522-5820. doi:10.1038/s42254-022-00552-1. URL <http://dx.doi.org/10.1038/s42254-022-00552-1>.
- [67] Ludmila Szulakowska and Jun Dai. Bayesian autotuning of hubbard model quantum simulators, 2022. URL <https://arxiv.org/abs/2210.03077>.
- [68] Oswin Krause, Bertram Brovang, Torbjørn Rasmussen, Anasua Chatterjee, and Ferdinand Kuemmeth. Estimation of convex polytopes for automatic discovery of charge state transitions in quantum dot arrays. *Electronics*, 11(15):2327, July 2022. ISSN 2079-9292. doi:10.3390/electronics11152327. URL <http://dx.doi.org/10.3390/electronics11152327>.
- [69] D. J. Reilly. Challenges in scaling-up the control interface of a quantum computer. In *2019 IEEE International Electron Devices Meeting (IEDM)*. IEEE, December 2019. doi:10.1109/iedm19573.2019.8993497. URL <http://dx.doi.org/10.1109/IEDM19573.2019.8993497>.
- [70] Pierre-Antoine Mouny, Raphaël Dawant, Bastien Galaup, Serge Ecoffey, Michel Pioro-Ladrière, Yann Beilliard, and Dominique Drouin. Analog programming of cmos-compatible al<sub>2</sub>o<sub>3</sub>/tio<sub>2</sub>-x memristor at 4.2k after metal-insulator transition suppression by cryogenic reforming. *Applied Physics Letters*, 123(16), October 2023. ISSN 1077-3118. doi:10.1063/5.0170058. URL <http://dx.doi.org/10.1063/5.0170058>.
- [71] Frédéric Marcotte, Pierre-Antoine Mouny, Victor Yon, Gebremedhin A. Dagnew, Bohdan Kulchytsky, Sophie Rochette, Yann Beilliard, Dominique Drouin, and Pooya Ronagh. A cryogenic memristive neural decoder for fault-tolerant quantum error correction, 2023. URL <https://arxiv.org/abs/2307.09463>.
- [72] Raphaël Dawant, Matthieu Gaudreau, Marc-Antoine Roy, Pierre-Antoine Mouny, Matthieu Valdenaire, Pierre Glielch, Javier Arias Zapata, Malek Zegaoui, Fabien Alibart, Dominique Drouin, and Serge Ecoffey. Damascene versus subtractive line cmp process for resistive memory crossbars beol integration. *Micro and Nano Engineering*, 23:100251, June 2024. ISSN 2590-0072. doi:10.1016/j.mne.2024.100251. URL <http://dx.doi.org/10.1016/j.mne.2024.100251>.
- [73] Dennis V Christensen, Regina Dittmann, Bernabe Linares-Barranco, Abu Sebastian, Manuel Le Gallo, Andrea Redaelli, Stefan Slesazek, Thomas Mikolajick, Sabina Spiga, Stephan Menzel, Ilia Valov, Gianluca Milano, Carlo Ricciardi, Shi-Jun Liang, Feng Miao, Mario Lanza, Tyler J Quill, Scott T Keene, Alberto Salleo, Julie Grollier, Danijela Marković, Alice Mizrahi, Peng Yao, J Joshua Yang, Giacomo Indiveri, John Paul Strachan, Suman Datta, Elisa Vianello, Alexandre Valentian, Johannes Feldmann, Xuan Li, Wolfram H P Pernice, Harish Bhaskaran, Steve Furber, Emre Neftci, Franz Scherr, Wolfgang Maass, Srikanth Ramaswamy, Jonathan Tapson, Priyadarshini Panda, Youngeun Kim, Gouhei Tanaka, Simon Thorpe, Chiara Bartolozzi, Thomas A Cleland, Christoph Posch, ShihChii Liu, Gabriella Panuccio, Mufti Mahmud, Arnab Neelim Mazumder, Morteza Hosseini, Tinoosh Mohsenin, Elisa Donati, Silvia Tolu, Roberto Galeazzi, Martin Ejsing Christensen, Sune Holm, Daniele Ielmini, and N Pryds. 2022 roadmap on neuromorphic computing and engineering. *Neuromorphic Computing*

- and Engineering*, 2(2):022501, May 2022. ISSN 2634-4386. doi:10.1088/2634-4386/ac4a83. URL <http://dx.doi.org/10.1088/2634-4386/ac4a83>.
- [74] Wei Wang, Wenhao Song, Peng Yao, Yang Li, Joseph Van Nostrand, Qinru Qiu, Daniele Ielmini, and J. Joshua Yang. Integration and co-design of memristive devices and algorithms for artificial intelligence. *iScience*, 23(12): 101809, December 2020. ISSN 2589-0042. doi:10.1016/j.isci.2020.101809. URL <http://dx.doi.org/10.1016/j.isci.2020.101809>.
- [75] Amirali Amirsoleimani, Fabien Alibert, Victor Yon, Jianxiong Xu, M. Reza Pazhouhandeh, Serge Ecoffey, Yann Beilliard, Roman Genov, and Dominique Drouin. In-memory vector-matrix multiplication in monolithic complementary metal–oxide–semiconductor-memristor integrated circuits: Design choices, challenges, and perspectives. *Advanced Intelligent Systems*, 2(11), August 2020. ISSN 2640-4567. doi:10.1002/aisy.202000115. URL <http://dx.doi.org/10.1002/aisy.202000115>.
- [76] Victor Yon, Bastien Galaup, Roger G. Melko, Yann Beilliard, and Dominique Drouin. Robust quantum dots charge autotuning using neural networks uncertainty - Output data, May 2024. URL <https://doi.org/10.5281/zenodo.11403192>.
- [77] Labelbox, Inc. Labelbox, 2024. URL <https://labelbox.com>.
- [78] Diederik P. Kingma and Jimmy Ba. Adam: A method for stochastic optimization, 2014. URL <https://arxiv.org/abs/1412.6980>.
- [79] Adam Paszke, Sam Gross, Francisco Massa, Adam Lerer, James Bradbury, Gregory Chanan, Trevor Killeen, Zeming Lin, Natalia Gimelshein, Luca Antiga, Alban Desmaison, Andreas Köpf, Edward Yang, Zach DeVito, Martin Raison, Alykhan Tejani, Sasank Chilamkurthy, Benoit Steiner, Lu Fang, Junjie Bai, and Soumith Chintala. Pytorch: An imperative style, high-performance deep learning library, 2019. URL <https://arxiv.org/abs/1912.01703>.
- [80] Piero Esposito. Blitz - bayesian layers in torch zoo (a bayesian deep learning library for torch), 2020. URL <https://github.com/piEsposito/blitz-bayesian-deep-learning>.
- [81] Vishal Thanvantri Vasudevan, Abhinav Sethy, and Alireza Roshan Ghias. Towards better confidence estimation for neural models. In *ICASSP 2019 - 2019 IEEE International Conference on Acoustics, Speech and Signal Processing (ICASSP)*. IEEE, May 2019. doi:10.1109/icassp.2019.8683359. URL <http://dx.doi.org/10.1109/ICASSP.2019.8683359>.
- [82] Dan Hendrycks and Kevin Gimpel. A baseline for detecting misclassified and out-of-distribution examples in neural networks, 2016. URL <https://arxiv.org/abs/1610.02136>.
- [83] Murat Sensoy, Lance Kaplan, and Melih Kandemir. Evidential deep learning to quantify classification uncertainty, 2018. URL <https://arxiv.org/abs/1806.01768>.
- [84] Marcin Możejko, Mateusz Susik, and Rafał Karczewski. Inhibited softmax for uncertainty estimation in neural networks, 2018. URL <https://arxiv.org/abs/1810.01861>.
- [85] Alex Simpkins, Raymond de Callafon, and Emanuel Todorov. Optimal trade-off between exploration and exploitation. In *2008 American Control Conference*. IEEE, jun 2008. doi:10.1109/ACC.2008.4586462. URL <https://doi.org/10.1109/ACC.2008.4586462>.

# Supplemental Materials: Robust quantum dots charge autotuning using neural networks uncertainty

## S1 Datasets

Dataset short name	Si-SG-QD	GaAs-QD	Si-OG-QD
Dataset full name	Silicon split gate quantum dot	Gallium arsenide quantum dot	Silicon overlapping gate quantum dot
Current measurement method	SET	QPC	SET
Pixel size	1 mV	2.5 mV	2 mV
Detection area offset	6 pixels	7 pixels	6 pixels
Prior line distance	30 mV	16 mV	30 mV
Prior line slope (0° = horizontal, 90° = vertical)	75°	45°	-10°
Use last line validation	No (not necessary)	Yes	Yes
Number of diagrams with transition line annotations (used for line detection training and test)	17	9	12
Number of diagrams with transition line and charge area annotations (used for autotuning test)	9	9	9
Number of patches (18 × 18 pixels each)	72,182	4349	48,081
Patches classes ratio (no-line / line)	33.6	3.3	8.2
References	[40]	[41]	[14]

Table S1: Summary of datasets specifications. SET and QPC respectively stand for single-electron transistor and quantum point contact.

### S1.1 Data selection

The stability diagrams used in this article are the result of experimental measurements done during prior studies on quantum dot (QD) devices [40, 41]. Thus, most of the measurements were not suitable for this work and a selection has been made. Only stability diagrams matching with the following criteria were included in the final datasets:

General criteria:

- All diagrams of the same dataset are measured on similar devices. Hardware difference is acceptable between datasets, but consistency is required for each independent training.
- Similar measurement step size between G1 and G2. A step size mismatch between the two measured gates makes pixel interpolation less reliable.
- Double QD diagrams are excluded.

Transition line detection patches datasets:

- At least one transition line visible, or partially visible, in the diagram.

Autotuning datasets:

- At least three transition lines visible, or partially visible, in the diagram.
- Clearly identifiable empty regime in the measured range (no line for at least 2 times the average space between visible lines).

## S1.2 Data processing

The long-term goal of this project is to implement an automated control-loop as close as possible from the quantum device. Thus, we want to keep the preprocessing on the input data minimal to avoid any computation overhead inside the cryogenic environment. This is why we do not compute the derivative on the patches, nor complex data processing such as proposed in Czischek et al. [22]. Furthermore, most statistical methods required a large space sample to be reliable, which is incompatible with our small patch measurements strategy.

To improve the convergence of the models, we normalized the input model between 0 and 1 based on the smallest and largest current value of each patch.

## S1.3 Diagram annotation

We manually annotated the transition lines and the charge regime areas using *Labelbox* [77] at the diagram level. When the transition lines were mixed with background noise, we used the derivative of the images to place more accurate annotations. We only annotate the lines that we could visually identify, we never fill the gap between two sections of a line, even when it was clear that was the continuity of the same transition.

The voltage space is segmented in charge regime areas annotated from 0 to 3 electrons, then the voltage space corresponding to more than 3 electrons is annotated as “4+”. The location of each area is deduced from the position of the transition lines and the knowledge that the empty regime is located at the bottom left of the images. When the regime of a section is ambiguous or difficult to identify (too noisy, fading line, few pixels around a line), no annotation is set, and the regime of this voltage space is considered as “*unknown*” during the experiment (examples in Figure 2e,f). When an autotuning ends in an “*unknown*” regime, it is always considered as a failure.

Annotating the transition lines and charge regimes of one stability diagram took 5 min to 30 min, depending on its complexity. It took approximately 10 h to annotate the 38 stability diagrams used in the study.

## S1.4 Patch segmentation and automatic class labeling

The patch size has been fixed at  $18 \times 18$  pixels as a tradeoff between measurement time and classifier performance. With a smaller patch size, it becomes difficult to distinguish a transition line from noise. A larger patch would directly increase the time required to measure it, reducing the exploration’s efficiency.

To train and test the neural networks (NNs), we split the diagrams into patches by swiping an  $18 \times 18$  window with 10 overlapping pixels between each step. We then automatically assign a class to every patch using the manual transition line annotations set previously (see section S1.3). If at least one line intersects with the detection area (Figure 3b), the patch is categorized as a “*line*”, otherwise, it is categorized as a “*no-line*”.

## S1.5 Subsets splitting

Every patch dataset is split into three subsets (mutually exclusive): training, validation, and test.

Each subset is used for a specific purpose:

**Training set** is used to train the line detection model.

**Validation set** is used after the training, to select the step corresponding to the best model (green stars in Figures S5) and to calibrate the confidence thresholds (Figures S6).

**Test set** is used to evaluate the line classification accuracy and the autotuning success rate, after the training and the calibration.

In the case of training with cross-validation (Figure S4), the subsets are split as follows:

**Training set** is composed of 90 % of the patches randomly selected among the train diagrams.

**Validation set** is composed of 10 % of the patches randomly selected among the train diagrams.

**Test set** is composed of every patch of the test diagram.

In the case of training without cross-validation:

**Training set** is composed of 70 % of the patches randomly selected among every diagram.



**Validation set** is composed of 10 % of the patches randomly selected among every diagram.

**Test set** is composed of 20 % of the patches randomly selected among every diagram.

### S1.6 Stability diagram samples

Every stability diagram used in this study can be downloaded from Yon et al. [43]. To illustrate the transition line annotation methodology and show the diagram diversity of each dataset, 2 diagrams of each dataset are presented in Figures S1, Figure S2, and Figure S3.

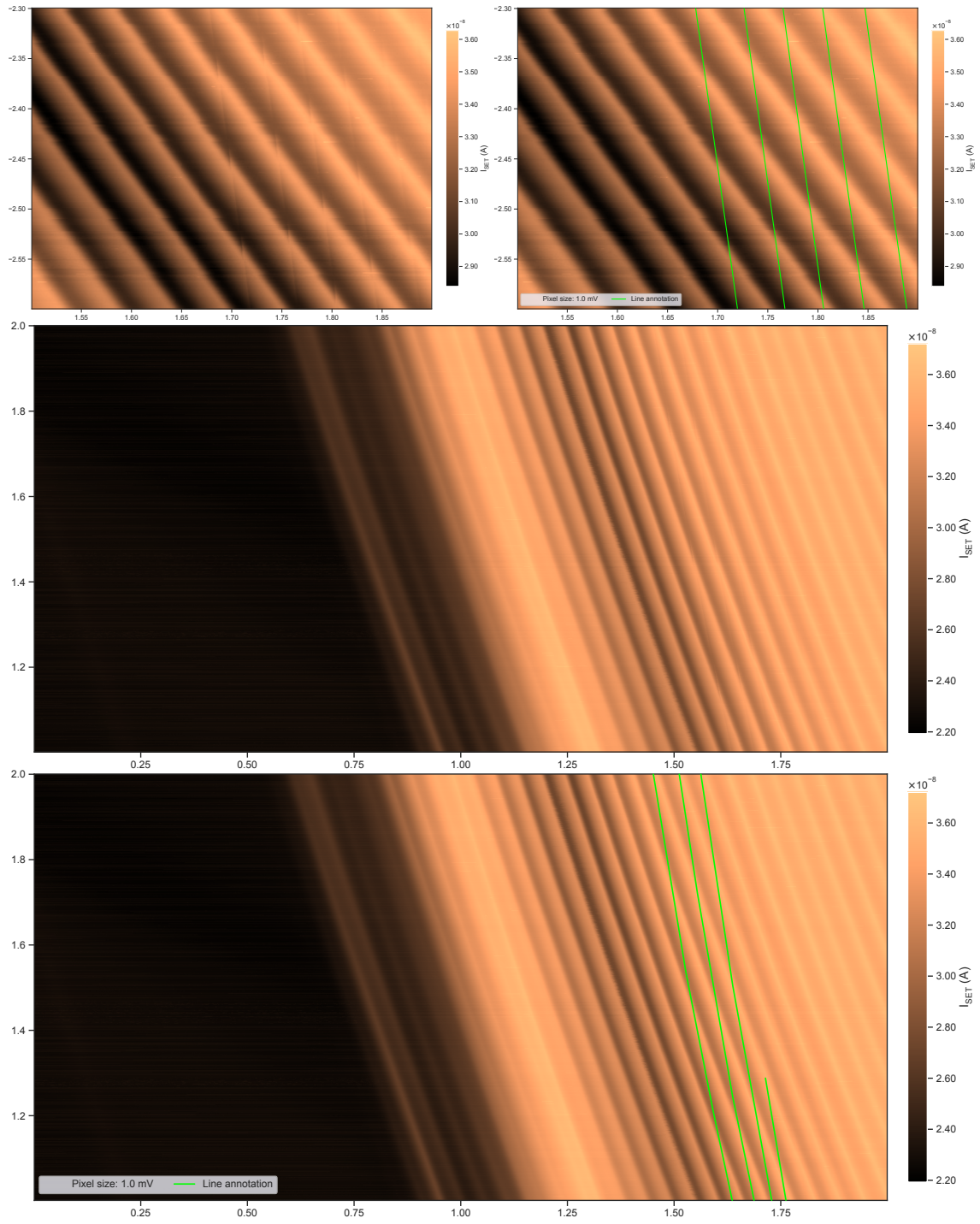


Figure S1: Two silicon split gate (Si-SG-QD) stability diagram examples, without and with transition line annotations. The  $x$ -axes correspond to the G1 gate voltage, and the  $y$ -axes correspond to the G2 gate voltage.

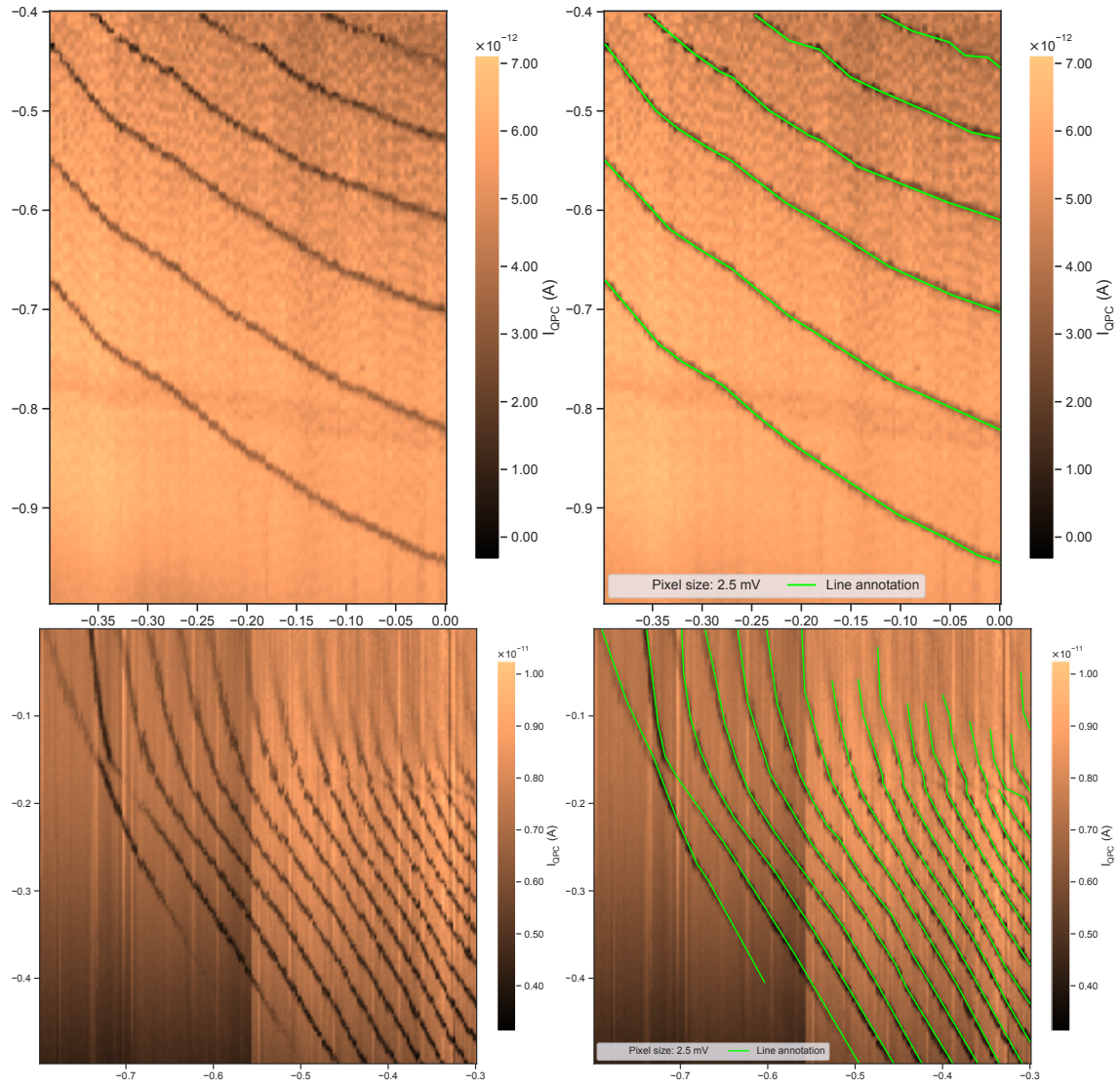


Figure S2: Two gallium arsenide (GaAs-QD) stability diagram examples, without and with transition line annotations. The  $x$ -axes correspond to the G1 gate voltage, and the  $y$ -axes correspond to the G2 gate voltage.

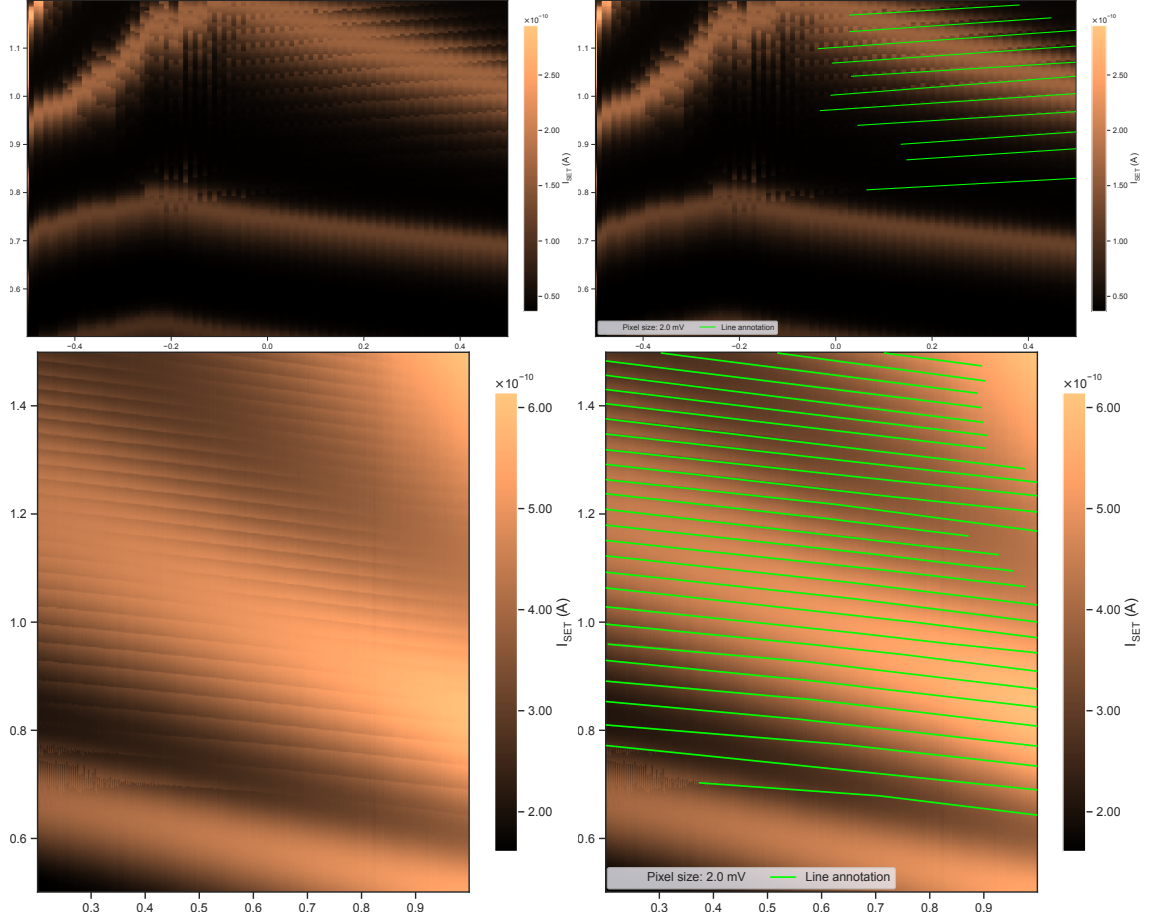


Figure S3: Two silicon overlapping gate (Si-OG-QD) stability diagram examples, without and with transition line annotations. The  $x$ -axes correspond to the G1 gate voltage, and the  $y$ -axes correspond to the G2 gate voltage.

## S2 Line detection methodology

Meta-parameters	FF	CNN	BCNN
Number of train updates	15,000	30,000	
Layers description	Fully connected: - 400 - 100	Convolutions: - kernel $4 \times 4$ , 12 channels - kernel $4 \times 4$ , 24 channels Fully connected: - 200 - 100	
Number of free parameters	170,201	367,267	734,534
Loss function	Binary cross-entropy		Binary cross-entropy + Complexity cost [53]
Optimizer	Adam [78]		
Learning rate	0.0005	0.001	
Dropout rate	60 %		0 %
Batch size	512		
Number of inference per patch ( $N$ in Equation 2)	1		10

Table S2: Models architectures and training meta-parameters used for this study.

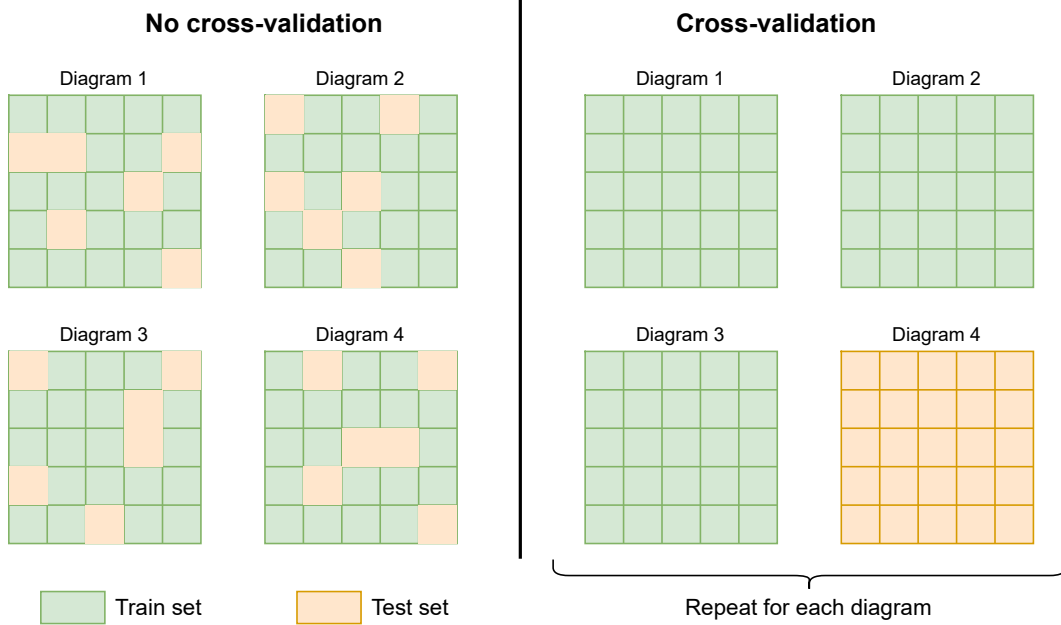


Figure S4: Digram cross-validation methodology schematic. The left panel represents the “No cross-validation” method, where every diagram is split into patches, then a random set of patches are used for training and the rest for testing. The right panel represents the “Cross-validation” method [62], where every diagram is split into patches, then the patched of one diagram are used for testing while the patches of the others are used for training. The process is repeated for every diagram and the performance is averaged.

### S2.1 Models training

Every NN is trained with PyTorch [79] v2.1 in a supervised manner. Bayesian convolutional neural networks (BCNNs) also used the *BLiTZ* library [80] to create the bayesian layers, sample the parameters and compute the parameters’ update with *Bayes-by-Backprop* [53]. The training parameters and the NN architectures are described in Table S2, the source code used to obtain the results presented in this article is available on Github <sup>1</sup>, and the output files (including trained model’s parameters) can be downloaded from Yon et al. [76].

The imbalanced classes ratio (“*line*” / “*no-line*”) caused convergence issues since the loss could be easily reduced by predicting only the most frequent class (“*no-line*”). We worked around this problem by re-balancing the patch dataset with weighted sampling for each batch.

The meta-parameters presented in Table S2 have been selected by grid search and informed guess. It is likely that these meta-parameters could be optimized and fine-tuned to improve the accuracy, accelerate the training and reduce the number of free parameters. However, the scope of this study is to demonstrate the feasibility of the autotuning procedure and the benefit of using model uncertainty, not to achieve the best possible performance.

<sup>1</sup>Git repository: <https://github.com/3it-inpaqt/dot-calibration-v2/tree/offline-article>

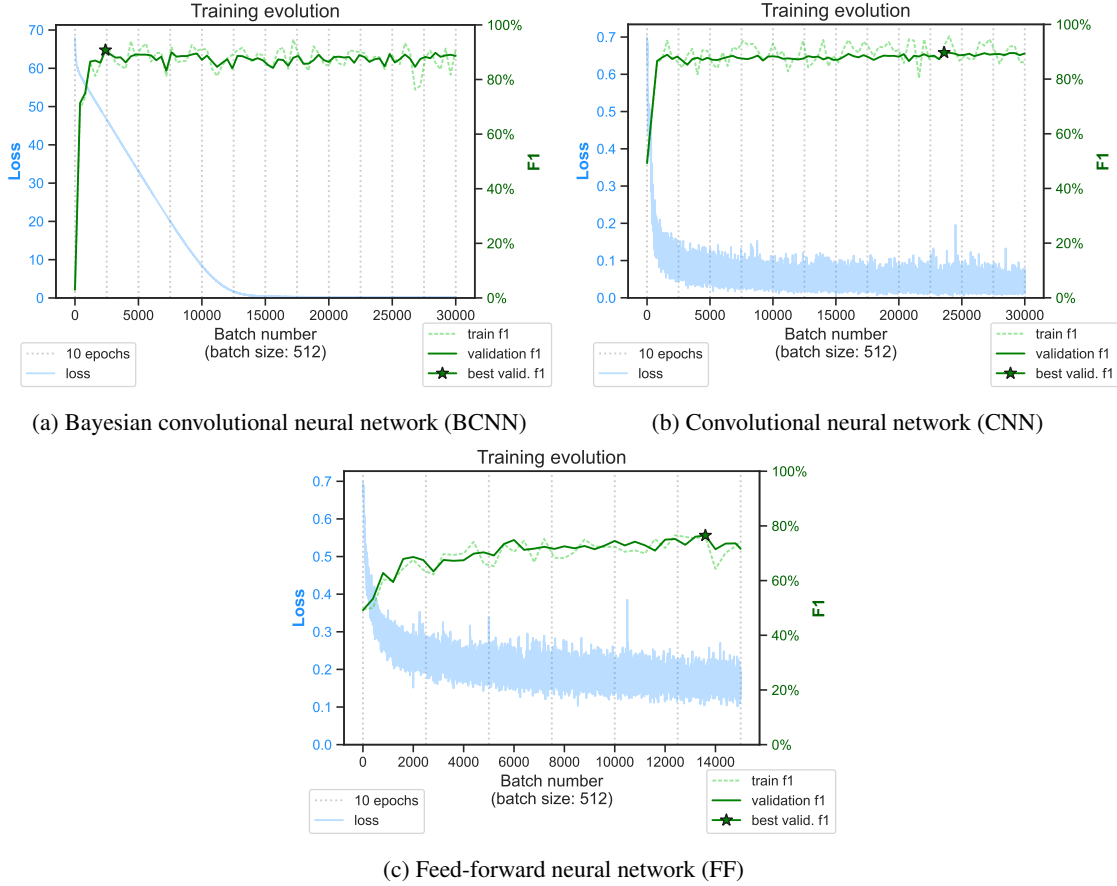


Figure S5: Examples of training progress for the silicon split gate (Si-SG-QD) dataset with the different models and the cross-validation method. The F1 score is the harmonic mean of the precision and recall.

## S2.2 Model uncertainty and confidence threshold calibration

To estimate and use NN uncertainty, we had to take three important decisions: what model to use, what confidence metric to compute, and how to define the confidence threshold under which the inference should not be considered reliable.

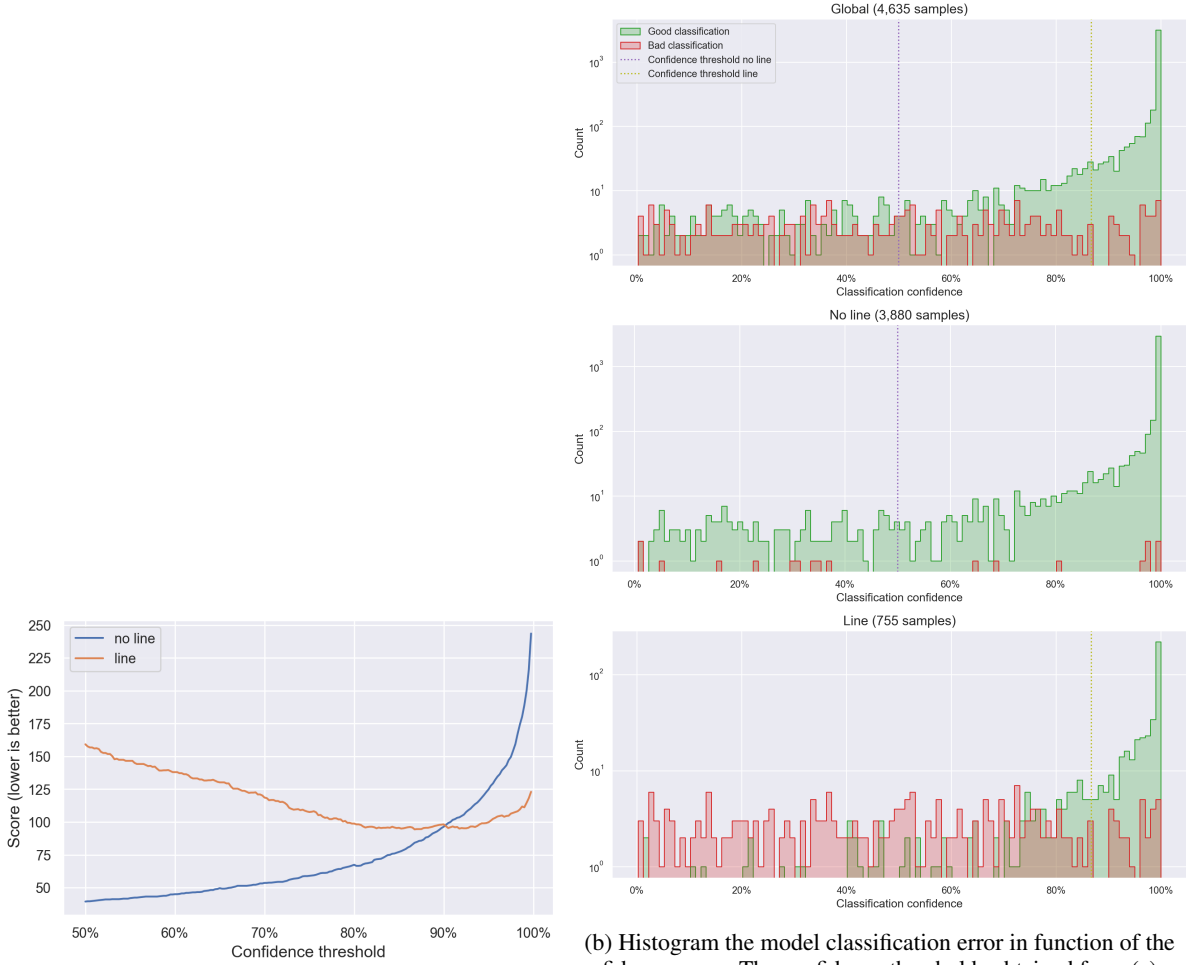
We evaluated a standard convolutional neural network (CNN) and feed-forward neural network (FF) as references, since they are the most simple and well established NNs for image pattern recognition. Such models are not specifically designed nor trained to estimate uncertainty. Several studies [81–84] suggested that classical NNs are generally overconfident and provide badly calibrated confidence scores. For the sake of simplicity, we defined the confidence score as the distance between the output and the closest class (Formula 1). This score is normalized between 0 and 1 to be easily interpretable and comparable as a confidence percentage.

We chose to implement a BCNN using variational inference [51, 52] and trained with Bayes-by-Backprop [53] method. This choice is motivated by previous promising results [49, 50], and the library [80] compatible with PyTorch [79]. The confidence score is computed as a normalized standard deviation (Formula 2) from 10 inferences of the same input with new parameters sampling.

A model is well calibrated if the confidence score accurately expresses the probability to make an error, for example, 20% of the classifications with 80% of confidence should be wrong. However, a trained NN is never perfectly calibrated, and the calibration task is challenging for several reasons. First, an NN training involves some stochastic process (parameters initialization, stochastic gradient descent, ...) that leads to different results, so two identical models trained separately could have very different and unpredictable miss-calibration issues. Secondly, within one model, each predicted class could necessitate independent calibration (Figures S6). We also suspect that the unbalanced class distribution of the dataset could amplify the problem. Finally, calibrating the confidence score with the training



set induces a bias since the out-of-distribution examples are (by definition) not represented. Expressing correctly the distributional uncertainty in the model score is critical, especially with the cross-validation testing method.



(a) Evolution of the threshold score (Formula 3) while the threshold is varied. The threshold with the lowest score value is selected as the optimal threshold for each class.

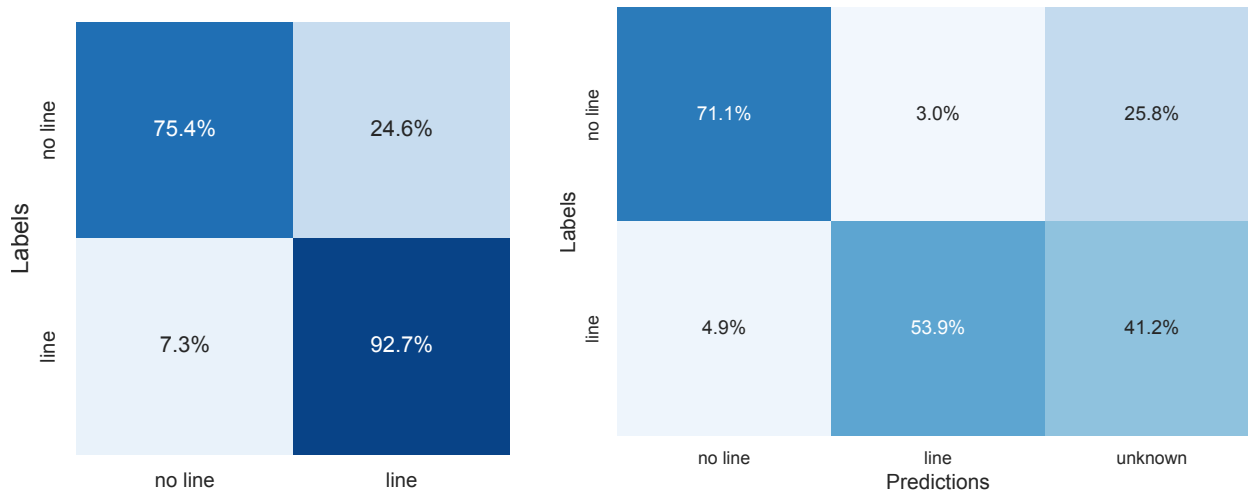
(b) Histogram the model classification error in function of the confidence score. The confidence thresholds obtained from (a) are represented by the vertical dot lines. The top panel shows the distribution for both classes combined, while the bottom panels show the distribution for each class independently.

Figure S6: Example of a confidence thresholds calibration for the silicon overlapping gate (Si-OG-QD) dataset with convolutional neural network (CNN) and the cross-validation method. The calibration of the thresholds is done after the training, on 4635 patches from the validation-set. The confidence threshold of each class is calibrated independently. The few number of classification errors for the “no-line” class in the validation-set make the calibration challenging. Therefore, the value of 50 % is used as a default minimal threshold.

Model calibration methods require enough samples to cover the whole confidence spectrum, which might be challenging with a limited dataset. For example, a model with high accuracy will correctly classify most of the samples with a high confidence score, implying that the samples in the low confidence intervals will be very sparse (e.g., in the middle panel of Figure S6b). Therefore, it is impossible to tell whether the model is under-confident or over-confident in these sparse intervals. Fortunately, the presented uncertainty-based exploration strategy does not require the exact probability of correctness for all the confidence ranges. The purpose of the confidence score in the context of this exploration task is to optimize the exploration-exploitation tradeoff [58, 85]. When a classification is done with a confidence score under the threshold, adjacent patches will be explored. If the algorithm explores too much, it may waste time on unnecessary measurements, leading to inefficiency. Conversely, if it exploits too soon, it risks making incorrect tuning decisions based on incomplete or inaccurate information. In other words, we want to reduce the number of errors (impacting the tuning success rate) relative to the number of patches scanned (impacting the tuning time). Calibrating the threshold value by minimizing the score defined by Formula 3 is a simple way to account for the exploration-exploitation tradeoff.

Fixing the meta-parameters  $\tau$  to 0.2 is equivalent to saying that we prefer to have up to 5 more patches scanned rather than having a classification error.

Other types of models, meta-parameters values, training methods, confidence scores, and calibration methods could be evaluated to address this autotuning problem. But an extensive benchmark of NNs uncertainty is out of the scope of this paper.

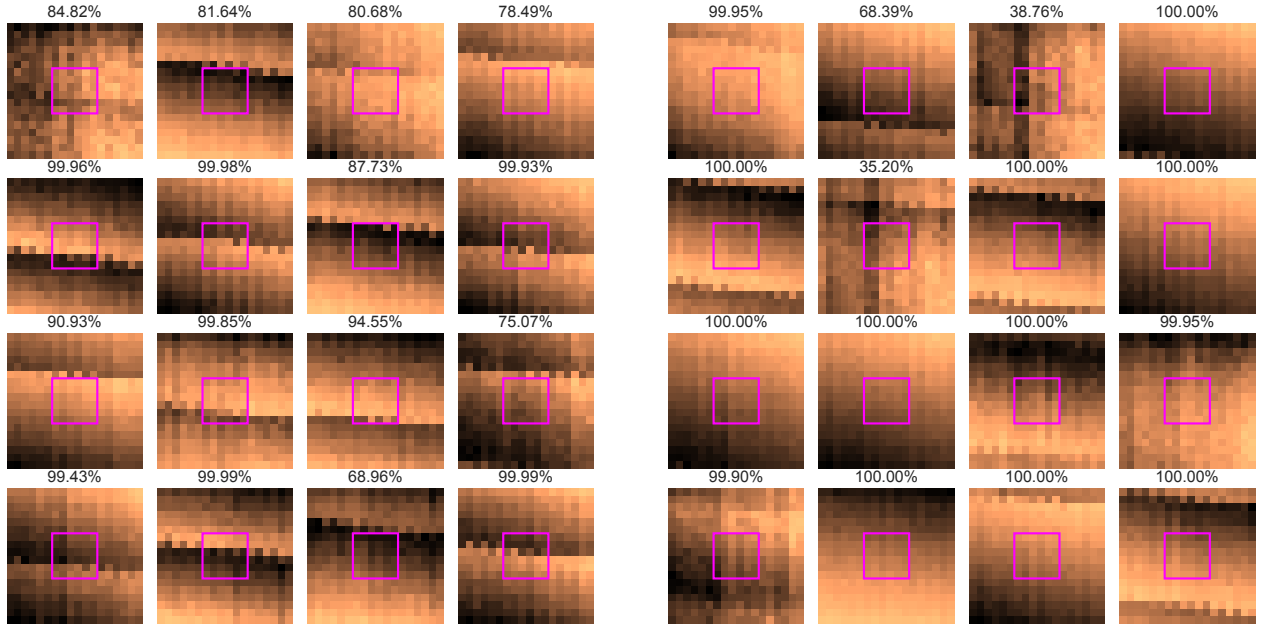


(a) Confusion matrix without using the confidence threshold. Accuracy: 81.5%, Precision: 81.0%, Recall: 84.1%, F1-score 80.9%.

(b) Confusion matrix where every classification with a confidence score below the threshold is considered as "unknown". Accuracy: 94.6%, Precision: 93.5%, Recall: 93.8%, F1-score 93.6%, Unknown rate 31.2%.

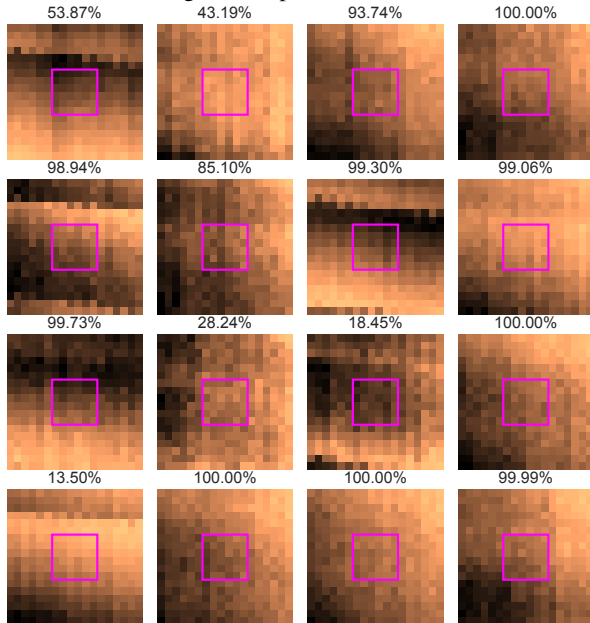
Figure S7: Example of a confusion matrix for the silicon overlapping gate (Si-OG-QD) dataset with convolutional neural network (CNN) and the cross-validation training method. Using the confidence threshold greatly improves the classification performance at the price of 31.2% patches set as "unknown".

### S2.3 Patch classification samples

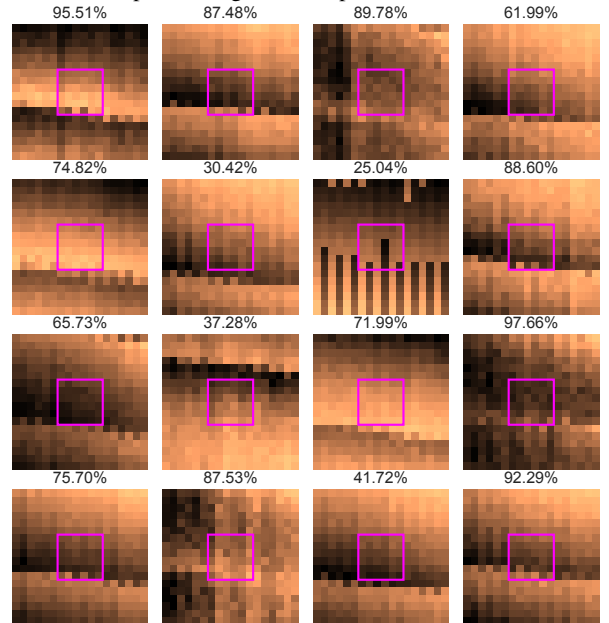


(a) Correctly classified patches labeled as “line”. 16 examples among the 947 patches in this case.

(b) Correctly classified patches labeled as “no-line”. 16 examples among the 1438 patches in this case.



(c) Badly classified patches as “no-line” (labeled as “line”). 16 examples among the 75 patches in this case.



(d) Badly classified patches as “line” (labeled as “no-line”). 16 examples among the 468 patches in this case.

Figure S8: Examples of patch classifications for the silicon overlapping gate (Si-OG-QD) dataset with a convolutional neural network (CNN) and the cross-validation training method. The patches are randomly selected among the test set. The pink squares in the center of patches correspond to the detection area. A patch is labeled as “line” only if a transition line annotation crosses this square. The percentages at the top of each patch correspond to the confidence scores of the CNN computed with the Formula 1.

The Figures S8 present examples of classification results to illustrate the line detection performance. We can observe that the classification errors (Figures S8c,d) are often due to the presence of a transition line close to the detection area

or annotation mistakes. In general, the confidence scores are lower when the patch is misclassified. More samples can be found in the simulation results files available for download from Yon et al. [76].

### S3 Autotuning methodology

#### S3.1 Exploration algorithm

The autotuning exploration algorithm is illustrated as a block diagram in Figure S9.

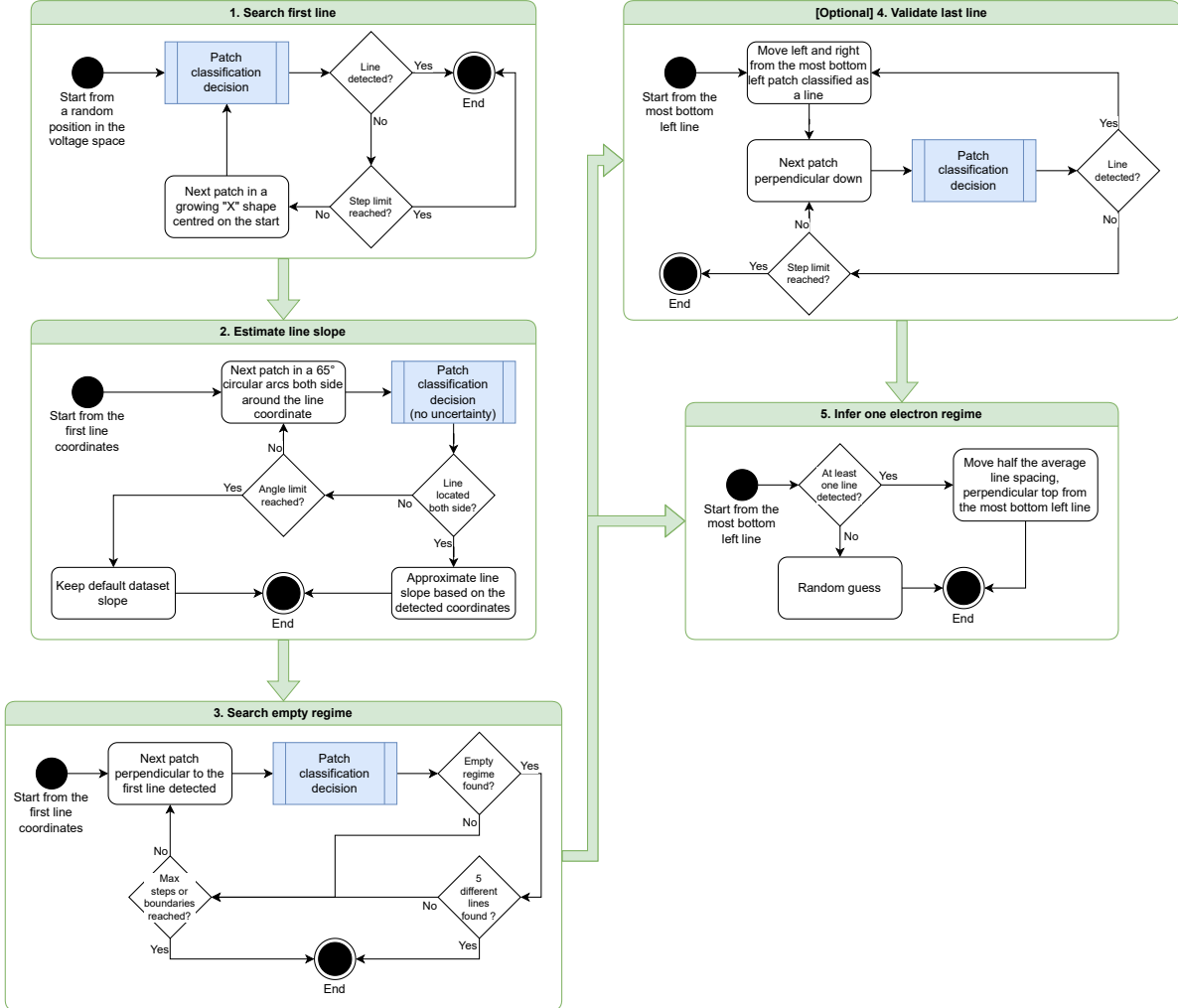


Figure S9: Detailed exploration strategy schematic, representing each step of the autotuning procedure. The optional *step 4* is enabled for the GaAs-QD and Si-OG-QD datasets to improve the tuning success rate when the first transition line is fading (examples in Figures S3).

#### Notes about the estimation of the transition line slope (step 2)

After finding the first patch containing a transition line, we scan and classify a sequence of patches in circular arcs (up to  $65^\circ$ ) on both sides around this location. This scan sequence is illustrated in step 2 of the Figure 5 (the white arrows emphasized the arc directions).

We consider an arc valid if we detect a sequence of patches matching the following pattern:

$$m \times \text{no-line}, n \times \text{line}, p \times \text{no-line}$$

Where  $m$ ,  $n$ , and  $p$  are positive integers representing the number of consecutive patches classified in the given label.

If both arcs are valid, we can estimate the coordinates of two points in the line by taking the position between the first and the last patch coordinates in the  $n$  sequence of each arc. With these two points and the *2-argument arctangent* function, we can extract the estimated slope value.

If at least one of the arcs is invalid (e.g., the line fades or a patch is misclassified), we keep the default slope value until the end of the run.

### S3.2 Baselines

Two simple baselines are used as reference to interpret and analyze the results of the autotuning simulations. The benchmark methodology is identical to the other autotuning procedures, including the repetition over 10 random seeds and 50 random starting points for each stability diagram.

The “*oracle*” baseline uses the exact same exploration logic that the one presented in the article, but the line detection model is replaced by an “*oracle*” which has access to the labels ground truth. Therefore, every patch classification is 100 % accurate with a maximal confidence score. This baseline allows us to isolate the tuning errors related to the exploration strategy from the ones caused by model misclassification. The results of this baseline corroborate the conclusion that the gallium arsenide (GaAs-QD) and silicon overlapping gate (Si-OG-QD) datasets are more challenging to explore. Possibly due to the transition line irregularities and unpredictable shapes.

The “*random*” baseline represents the worst case of exploration, where a pair of coordinates is randomly selected inside the voltage space of the tuned stability diagram. The success rate of this baseline can be interpreted as the one-electron regime area average surface of the dataset’s diagrams. A larger surface is expected to be easier to find by an autotuning procedure.

Therefore, these two baselines defined the minimal and maximal tuning success rate and average number of steps expected for each dataset.

Dataset	Baseline	Average step number	Tuning success
Si-SG-QD	oracle	151	100.0% $\pm 0.1$
	random	0	11.8% $\pm 1.5$
GaAs-QD	oracle	94	96.7% $\pm 0.6$
	random	0	10.1% $\pm 1.4$
Si-OG-QD	oracle	164	92.0% $\pm 0.9$
	random	0	5.3% $\pm 1.0$

Table S3: Autotuning results with “*oracle*” and “*random*” baselines. Variability over 10 random seeds.

## S4 Results without cross-validation

The performance loss observed while using the cross-validation method (illustrated in Figure S4) gives us an insight into the effect of the distributional uncertainty on the autotuning success rate. The results of the line detection model trained without cross-validation, presented in Table S4, show a high accuracy for every dataset (above 98 % when using the uncertainty threshold) and a rate below threshold (number of patches classified as “*unknown*”) consistently lower than with cross-validation (presented in Table 1). As shown in Table S5, the autotuning success rates directly benefit from the model performance gain. This gap is even greater when the dataset contains very different diagrams, such as the GaAs-QD dataset. Therefore, reducing the distributional uncertainty seems to be a promising way to improve the autotuning success rate. Which could be archived either by covering a boarder range of diagrams in the training set or by reducing the device fabrication variability.

Dataset	Model	Accuracy	Accuracy above threshold	Error reduction using threshold	Rate below threshold
Si-SG-QD	BCNN	98.8% $\pm$ 0.1	<b>99.8%</b> $\pm$ 0.1	79.9% $\pm$ 5.1	2.0% $\pm$ 0.3
	CNN	98.7% $\pm$ 0.1	<b>99.8%</b> $\pm$ 0.1	86.4% $\pm$ 3.6	2.0% $\pm$ 0.2
	FF	96.5% $\pm$ 0.7	<b>99.8%</b> $\pm$ 0.1	92.9% $\pm$ 3.1	10.7% $\pm$ 2.3
GaAs-QD	BCNN	94.3% $\pm$ 0.9	96.9% $\pm$ 1.1	46.5% $\pm$ 15.9	8.0% $\pm$ 3.1
	CNN	95.2% $\pm$ 0.7	<b>98.0%</b> $\pm$ 0.9	59.7% $\pm$ 14.3	7.5% $\pm$ 2.6
	FF	93.9% $\pm$ 1.1	97.6% $\pm$ 0.8	60.9% $\pm$ 10.0	10.5% $\pm$ 2.4
Si-OG-QD	BCNN	95.3% $\pm$ 0.3	98.4% $\pm$ 0.2	65.8% $\pm$ 5.8	7.4% $\pm$ 1.4
	CNN	93.6% $\pm$ 0.4	<b>99.1%</b> $\pm$ 0.2	85.2% $\pm$ 2.3	11.4% $\pm$ 0.9
	FF	94.1% $\pm$ 0.3	98.9% $\pm$ 0.2	81.0% $\pm$ 3.0	11.1% $\pm$ 0.7

Table S4: Line detection results, without cross-validation, for each dataset and model. The performances are averaged over 10 runs with different random seeds. The standard deviation of the runs’ performances represents the variability of the methods. Each run covers every diagram of the dataset. The best test accuracy scores of each dataset are highlighted in bold.

Dataset	Model	Line detection accuracy	Uncertainty-based tuning	Average step number	Tuning success
Si-SG-QD	BCNN	98.8% $\pm$ 0.1	Yes	166	99.5% $\pm$ 0.3
			No	151	92.2% $\pm$ 2.7
	CNN	98.7% $\pm$ 0.1	Yes	166	<b>99.9%</b> $\pm$ 0.2
			No	152	91.2% $\pm$ 3.5
			Yes	199	71.2% $\pm$ 11.7
			No	128	30.7% $\pm$ 15.0
GaAs-QD	BCNN	94.3% $\pm$ 0.9	Yes	101	85.4% $\pm$ 9.9
			No	93	66.2% $\pm$ 6.8
	CNN	95.2% $\pm$ 0.7	Yes	100	<b>92.2%</b> $\pm$ 2.5
			No	95	85.8% $\pm$ 5.5
			Yes	104	78.0% $\pm$ 5.6
			No	92	63.0% $\pm$ 3.8
Si-OG-QD	BCNN	95.3% $\pm$ 0.3	Yes	184	81.8% $\pm$ 2.3
			No	160	70.2% $\pm$ 3.5
	CNN	93.6% $\pm$ 0.4	Yes	189	84.3% $\pm$ 3.0
			No	153	61.7% $\pm$ 4.3
			Yes	194	<b>85.0%</b> $\pm$ 1.1
			No	154	65.5% $\pm$ 2.4

Table S5: Autotuning results for each dataset and model without cross-validation. With and without using the model uncertainty information provided by the confidence score. The line detection accuracy and tuning success variability are computed over 10 runs with different random seeds. Each run covers every diagram of the dataset. The best tuning success rates of each dataset are highlighted in bold.